

Hyper Suprime-Cam Year 3 results: Measurements of clustering of SDSS-BOSS galaxies, galaxy-galaxy lensing, and cosmic shear

Surhud More^{1,2} Sunao Sugiyama^{2,3} Hironao Miyatake^{4,5,2} Markus Michael Rau^{6,7} Masato Shirasaki^{8,9}
 Xiangchong Li^{7,2} Atsushi J. Nishizawa^{10,11} Ken Osato^{12,13} Tianqing Zhang⁷ Masahiro Takada²
 Takashi Hamana¹⁴ Ryuichi Takahashi¹⁵ Roohi Dalal¹⁶ Rachel Mandelbaum⁷ Michael A. Strauss¹⁶
 Yosuke Kobayashi^{17,2} Takahiro Nishimichi^{18,2,19} Masamune Oguri^{12,13} Wentao Luo^{20,21} Arun Kannawadi¹⁶
 Bau-Ching Hsieh²² Robert Armstrong²³ James Bosch¹⁶ Yutaka Komiyama²⁴ Robert H. Lupton¹⁶
 Nate B. Lust¹⁶ Lauren A. MacArthur¹⁶ Satoshi Miyazaki²⁵ Hitoshi Murayama^{26,27,2} Yuki Okura¹⁴
 Paul A. Price¹⁶ Philip J. Tait²⁵ Masayuki Tanaka¹⁴ and Shiang-Yu Wang²²

¹*The Inter-University Centre for Astronomy and Astrophysics, Post bag 4, Ganeshkhind, Pune 411007, India*

²*Kavli Institute for the Physics and Mathematics of the Universe (WPI), The University of Tokyo Institutes for Advanced Study (UTIAS), The University of Tokyo, Chiba 277-8583, Japan*

³*Department of Physics, The University of Tokyo, Bunkyo, Tokyo 113-0031, Japan*

⁴*Kobayashi-Maskawa Institute for the Origin of Particles and the Universe (KMI), Nagoya University, Nagoya, 464-8602, Japan*

⁵*Institute for Advanced Research, Nagoya University, Nagoya 464-8601, Japan*

⁶*High Energy Physics Division, Argonne National Laboratory, Lemont, Illinois 60439, USA*

⁷*McWilliams Center for Cosmology, Department of Physics, Carnegie Mellon University, Pittsburgh, Pennsylvania 15213, USA*

⁸*National Astronomical Observatory of Japan, Mitaka, Tokyo 181-8588, Japan*

⁹*The Institute of Statistical Mathematics, Tachikawa, Tokyo 190-8562, Japan*

¹⁰*Gifu Shotoku Gakuen University, Gifu 501-6194, Japan*

¹¹*Institute for Advanced Research/Kobayashi Maskawa Institute, Nagoya University, Nagoya 464-8602, Japan*

¹²*Center for Frontier Science, Chiba University, Chiba 263-8522, Japan*

¹³*Department of Physics, Graduate School of Science, Chiba University, Chiba 263-8522, Japan*

¹⁴*National Astronomical Observatory of Japan, National Institutes of Natural Sciences, Mitaka, Tokyo 181-8588, Japan*

¹⁵*Faculty of Science and Technology, Hirosaki University, 3 Bunkyo-cho, Hirosaki, Aomori 036-8561, Japan*

¹⁶*Department of Astrophysical Sciences, Princeton University, Princeton, New Jersey 08544, USA*

¹⁷*Department of Astronomy/Steward Observatory, University of Arizona, 933 North Cherry Avenue, Tucson, Arizona 85721-0065, USA*

¹⁸*Center for Gravitational Physics and Quantum Information, Yukawa Institute for Theoretical Physics, Kyoto University, Kyoto 606-8502, Japan*

¹⁹*Department of Astrophysics and Atmospheric Sciences, Faculty of Science, Kyoto Sangyo University, Motoyama, Kamigamo, Kita-ku, Kyoto 603-8555, Japan*

²⁰*School of Physical Sciences, University of Science and Technology of China, Hefei, Anhui 230026, China*

²¹*CAS Key Laboratory for Researches in Galaxies and Cosmology/Department of Astronomy, School of Astronomy and Space Science, University of Science and Technology of China, Hefei, Anhui 230026, China*

²²*Academia Sinica Institute of Astronomy and Astrophysics, No. 1, Sec. 4, Roosevelt Road, Taipei 10617, Taiwan*

²³*Lawrence Livermore National Laboratory, Livermore, California 94551, USA*

²⁴*Department of Advanced Sciences, Faculty of Science and Engineering, Hosei University, 3-7-2 Kajino-cho, Koganei-shi, Tokyo 184-8584, Japan*

²⁵*Subaru Telescope, National Astronomical Observatory of Japan, 650 N Aohoku Place, Hilo, Hawaii 96720, USA*

²⁶*Berkeley Center for Theoretical Physics, University of California, Berkeley, California 94720, USA*

²⁷*Theory Group, Lawrence Berkeley National Laboratory, Berkeley, California 94720, USA*



(Received 6 April 2023; accepted 25 September 2023; published 11 December 2023)

We utilize the Sloan Digital Sky Survey Baryon Oscillation Spectroscopic Survey (SDSS-BOSS) galaxies and its overlap with approximately 416 sq degrees of deep *grizy*-band imaging from the Subaru Hyper Suprime-Cam Survey (HSC). We perform measurements of three two-point correlations which form the basis of the cosmological inference presented in our companion papers, Miyatake *et al.* and Sugiyama *et al.* We use three approximately volume limited subsamples of spectroscopic galaxies by their *i*-band magnitude from the SDSS-BOSS: LOWZ ($0.1 < z < 0.35$), CMASS1 ($0.43 < z < 0.55$) and CMASS2 ($0.55 < z < 0.7$), respectively. We present high signal-to-noise ratio measurements of the projected correlation functions of these galaxies, which is expected to be proportional to the projected matter correlation function on large scales with a proportionality constant dependent on the bias of galaxies. In order to help break the degeneracy between the amplitude of the matter correlation and the bias of these spectroscopic galaxies, we use the distortions of the shapes of fainter galaxies in HSC due to weak gravitational lensing, to measure the galaxy-galaxy lensing signal, which probes the projected galaxy-matter cross-correlation function of the SDSS-BOSS galaxies. We also measure the cosmic shear correlation functions from HSC galaxies which is related to the projected matter correlation function. We demonstrate the robustness of our measurements by subjecting each of them to a variety of systematic tests. Our use of a single sample of HSC source galaxies is crucial to calibrate any residual systematic biases in the inferred redshifts of our galaxies. We also describe the construction of a suite of mocks: (i) spectroscopic galaxy catalogs which obey the clustering and abundance of each of the three SDSS-BOSS subsamples, and (ii) galaxy shape catalogs which obey the footprint of the HSC survey and have been appropriately sheared by the large-scale structure expected in a Λ Cold Dark Matter model. We use these mock catalogs to compute the covariance of each of our observables.

DOI: [10.1103/PhysRevD.108.123520](https://doi.org/10.1103/PhysRevD.108.123520)

I. INTRODUCTION

The concordance cosmological model, Λ Cold Dark Matter (Λ CDM), is rooted in its ability to accurately describe a variety of cosmological observations. Primary among these are the statistics of anisotropies in the cosmic microwave background (CMB), e.g., [1,2], the distance-redshift relation obtained using type-Ia supernovae, e.g., [3] and baryon acoustic oscillations, e.g., [4–6], the abundance of galaxy clusters, e.g., [7,8], the redshift space clustering of galaxies, e.g., [9–11], and the weak gravitational lensing signal, e.g., [12–20]. The presence of dark matter and dark energy is essential to the success of the model, in which dark matter causes density fluctuations to grow due to gravitational instabilities, while dark energy causes an accelerated expansion at late times, e.g., [21]. Although the evidence for the presence of dark matter and dark energy in the Universe is quite compelling, their existence is a grand challenge to our current understanding of the physics of the Universe. The empirical characterization of the abundance of dark matter, the growth in its density fluctuations, and the behavior of the equation of state for dark energy can aid in the understanding of these components.

The measurements of density fluctuations in the early Universe have been mapped by CMB experiments such as Wilkinson Microwave Anisotropy Probe (WMAP) [22] and Planck [2]. These precise observations suggest that our Universe can be described as a simple flat Λ cold dark matter model with only a handful of parameters. Under the assumptions of this simple model, the CMB observations predict the value of σ_8 , which characterizes the root mean

square dispersion in the density fluctuations when averaged in spheres of radius $8h^{-1}$ Mpc today. This quantity can be directly inferred from observables in the Universe at late times.

The current observational frontier in this area is driven by Stage III dark energy experiments which are designed to probe dark energy and dark matter. The Kilo-Degree Survey [23,24], the Dark Energy Survey [25,26] and the Hyper Suprime-Cam survey Subaru Strategic Program (HSC) [27,28] have all conducted complementary galaxy imaging surveys that target multiple probes in order to address key questions related to dark matter and dark energy. Although these surveys use a combination of probes to address cosmology, gravitational lensing is the primary tool of interest. The images of background galaxies get sheared in a coherent manner due to the presence of intervening matter distribution between them and us, e.g., [29]. The correlation of these coherent distortion patterns, commonly called the cosmic shear signal, is related to the projected matter density distribution and is therefore sensitive to the cosmological parameters. The amplitude of this signal and its variation with redshift can be used to infer the growth of structure in dark matter and constrain the parameter combination $S_8 = \sigma_8 \Omega_m^{0.5}$, where Ω_m is the matter density parameter.

The clustering of galaxies can also be used to probe the large-scale structure of the Universe, as galaxies trace the matter distribution, e.g., [30]. Galaxies form within dark matter halos which are biased tracers of the matter distribution, e.g., [31], and the galaxy bias, b , is expected to depend upon the halo bias of their parent halos

[e.g. [32]]. On large scales this bias is expected to be linear, and the clustering of galaxies thus reflects the shape of the matter correlation function, ξ_{mm} . Such observations can therefore constrain cosmological parameters that determine the shape of ξ_{mm} , but its amplitude is entirely degenerate with galaxy bias, e.g., [33]. The dependence of the halo bias on the mass of the dark matter halo is further a function of the cosmological parameters, especially Ω_{m} and σ_8 , e.g., [34]. Therefore, the amplitude of the matter correlation function can be inferred if dark matter halo masses can be measured for galaxies using the galaxy-galaxy lensing [33,35,36]. The galaxy-galaxy lensing signal is the cross correlation of lens galaxy positions with shapes of background galaxies. Thus together a combination of the clustering measurements and small-scale lensing measurements can help infer cosmological constraints, e.g., [18,33,35,37–39]. Another avenue to use galaxy-galaxy lensing is to only focus on large scales so that the cosmological inference is not affected by issues related to galaxy assembly bias, e.g., [40]. The galaxy-galaxy lensing signal depends upon the halo matter cross-correlation, which on large scales is proportional to $b\xi_{\text{mm}}$. The large-scale clustering of galaxies is sensitive to $b^2\xi_{\text{mm}}$. Thus together they can help determine both the amplitude and shape of the matter correlation function.

The cosmological parameter dependences of cosmic shear or the combination of galaxy clustering and galaxy-galaxy lensing signal are expected to be different and thus complementary. Thus a combination of all the three two-point correlations can further reduce the uncertainties on the inferred cosmological parameters; see e.g. [14,20]. The first step in the careful inference of the cosmological parameters from these observables is the reliable measurement of the observables and their covariance. There is a variety of systematics that can affect each of these measurements; decisions need to be taken regarding the scales over which the signals can be reliably modeled as well as a demonstration that the measurements pass a variety of null tests. Inference of the redshift distribution of source galaxies is yet another step before the weak lensing measurements can be reliably modeled.

This is the first paper in a series of the 3×2 pt cosmology analyses of the Subaru HSC Year 3 data (hereafter HSC-Y3). In this paper (Paper I), we define the lens and source galaxy samples to be used for the 3×2 pt cosmological analyses. We present measurements of the three two-point functions as well as the results of various systematic tests which allow us to narrow down the scales to be used for cosmological analysis. We also present mock galaxy catalogs and shear catalogs that were used to obtain the covariance matrix of our measurements. The inference of the cosmological parameters was performed in a blind manner using these measurements, and those results will be presented in Miyatake *et al.* [[41], Paper II] and Sugiyama *et al.* [[42], Paper III], respectively. Paper II will use information on quasilinear scales by using the emulator-

based halo model, while the analysis in Paper III is based on linear scales where a model based on perturbation theory can be used reliably. The measurement and the cosmological analysis of the cosmic shear tomography in real space and Fourier space will be presented in companion papers, Li *et al.* [43] and Dalal *et al.* [44], respectively.

This paper is organized as follows. In Sec. II, we describe the HSC three-year shear catalog and the Sloan Digital Sky Survey Baryon Oscillation Spectroscopic Survey (SDSS-III BOSS) data that we use, our blinding strategy, the construction of the lens galaxy sample, as well as the construction of the mock galaxy catalogs which are used to determine the covariance of our measurements. In Sec. III, we present a brief description of our pipelines that we use to measure the galaxy clustering, the galaxy-galaxy lensing signal and the cosmic shear signal from our data. In Sec. IV, we present the measurements of the galaxy clustering signal, its covariance and a variety of systematic tests designed to assess the robustness of our measurements. In Sec. V, we present the measurements of the galaxy-galaxy lensing signal, its covariance, and a variety of null and systematic tests. In Sec. VI, we similarly present the measurements of the cosmic shear correlation functions and its covariance, the systematic tests as well as various Point Spread Function (PSF) related systematic tests. Finally, we summarize our results in Sec. VII.

When performing the galaxy clustering and galaxy-galaxy lensing analyses, we adopt a fiducial flat Λ CDM cosmological model with parameters consistent with the cosmic microwave background analysis from WMAP9. The cosmological model is specified by the CDM density parameter $\Omega_{\text{cdm}} = 0.233$, the baryon density $\Omega_{\text{b}0} = 0.046$, the matter density $\Omega_{\text{m}} = \Omega_{\text{cdm}} + \Omega_{\text{b}} = 0.279$, the cosmological constant $\Omega_{\Lambda} = 0.721$, the Hubble parameter $h = 0.7$, the amplitude of density fluctuations $\sigma_8 = 0.82$, and the spectral index $n_s = 0.97$. The choice of these cosmological parameters is dictated by the cosmological parameters adopted for the simulations that form the basis of the mock catalogs that we use for our covariance calculations [45]. While carrying out our cosmological analyses in Papers II and III, we will account for the cosmological dependence of our observables, so that our choice of this fiducial cosmological model has no impact on our cosmological inference.

II. DATA

The 3×2 pt cosmological analyses for HSC-Y3 data will focus on a combination of probes: the cosmic shear signal, the clustering of galaxies and their galaxy-galaxy lensing signal. In this section, we describe the data we use for the gravitational lensing measurements (Sec. II A), our blinding strategy (Sec. II B), the galaxy samples used for the clustering and the galaxy-galaxy lensing analyses (Sec. II C) as well as the mock catalogs that are used to estimate the covariance of these measurements (Sec. II D).

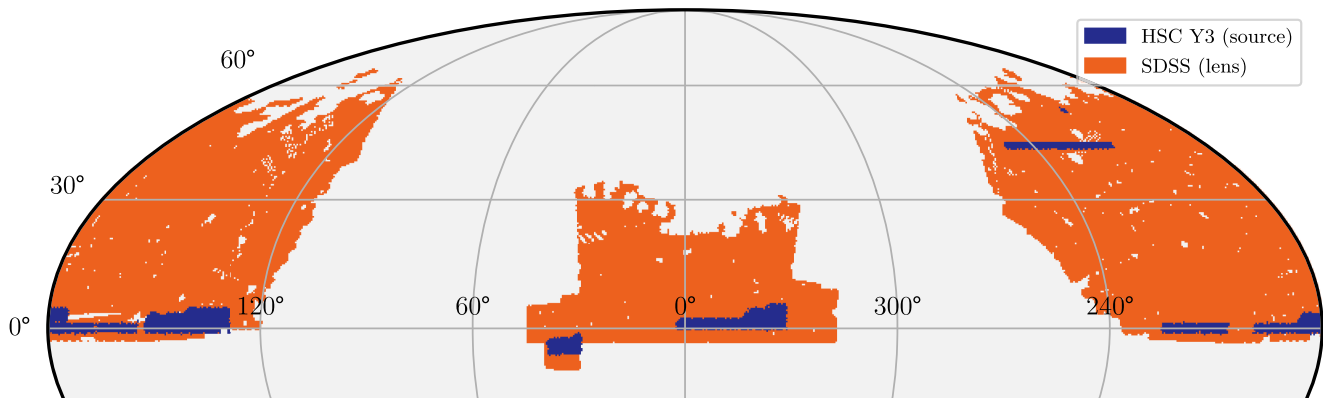


FIG. 1. The area coverage of the data used in this paper for performing 3×2 pt measurements. The catalog of HSC galaxies used for the weak lensing measurements is shown using the purple shaded region, while the catalog of SDSS galaxies is shown using yellow. The overlap between the two catalogs is ~ 416 sq degrees. Our measurement of the clustering signal uses the entire SDSS region, while the measurements of the galaxy-galaxy lensing signal and the cosmic shear signal utilize source galaxies in the overlapping area.

A. Shape catalog

The HSC instrument is a wide-field optical imaging camera mounted at the prime focus of the 8.2-meter Subaru Telescope [46–49]. The wide field of view combined with the excellent seeing conditions at Maunakea and the large aperture make it an ideal telescope for surveys targeting weak lensing measurements of a large-scale structure. The HSC-Subaru Strategic Program was allocated 330 nights to carry out a three-layered imaging survey in multiple bands with different depths [27]. The wide layer, which is designed for weak lensing cosmology, consists of multi-band *grizy* imaging that will cover an area of approximately 1100 deg^2 , upon completion. The galaxy shape measurements are carried out in the *i* band which is observed at a $5\text{-}\sigma$ depth of $i \sim 26$ ($2''$ aperture for a point source). The images in the *i* band were preferentially taken under good seeing conditions, which resulted in a median seeing of about 0.6 arcsec.

The data from the survey have been processed using a fork of Rubin’s LSST Science Pipelines catered to images taken with HSC [50], and which is updated from time to time to include new features, any bug fixes, and improvements to deal with the Subaru HSC data. The Subaru HSC survey has made three public data releases (PDR) thus far [51–53]. In this paper, we use the shape catalog from the S19a internal data release intermediate to PDR2 and PDR3, which was processed with *hscPipe* v7 [54]. There were a number of improvements to the PSF modeling, image warping kernel, background subtraction and bright star masks, which have improved the quality of the shape catalog in HSC-Y3 compared with the Year 1 shape catalog [55,56]. The detailed selection of galaxies that form the shape catalog is presented in Li *et al.* [54]. Briefly, the shape catalog consists of galaxies selected from the full-depth and full-color region in all five filters. Apart from some basic quality cuts related to pixel level information, we select extended objects with an extinction corrected

cmodel magnitude $i < 24.5$, *i*-band SNR ≥ 10 , resolution > 0.3 , $> 5\sigma$ detection in at least two bands other than *i*, a 1 arcsec diameter aperture magnitude cut of $i < 25.5$, and a blendedness cut in the *i* band of $10^{-3.8}$.

The shape catalog consists of a total of 35.7 million galaxies spanning an area of about 433 sq deg , an effective number density of 19.9 arcmin^{-2} . It is divided into six disjoint regions: XMM, VVDS, GAMA09H, WIDE12H, GAMA15H and HECTOMAP fields; see Fig. 2 in [54]. The shape measurements in the catalog were calibrated using detailed image simulations, such that the galaxy property dependent multiplicative shear estimation bias is less than $\sim 10^{-2}$. Li *et al.* [54] also presented a number of systematic tests and null tests, and quantified the level of residual systematics in the shape catalog that could affect the cosmological science analyses carried out using the data. Given that Li *et al.* [54] flag residual additive biases due to PSF model shape residual correlations and star galaxy shape correlations as systematics requiring special attention and marginalization, we will also investigate the effect of these systematics on the cosmic shear measurements.

As shown in Appendix D, we exclude a $\sim 20 \text{ sq degree}$ patch of the sky in the GAMA09H region from our analysis. This region was a significant source of *B*-mode systematics in the cosmic shear analysis presented in our companion paper Li *et al.* [43]. The resultant area of our shape catalog is $\sim 416 \text{ sq degrees}$. The on-sky projection of this area is shown in Fig. 1, as the purple shaded region.

The HSC-Y3 shape catalog is accompanied by a photometric redshift catalog of galaxies based on three different methods [57,58]. The software *Mizuki* is a template fitting based photometric redshift estimate code, while *DEmPz* and *DNNZ* provide machine learning based estimates of the photometric redshifts of galaxies [59]. Each of these methods provides an estimate of the posterior distribution function of the redshift for each galaxy, denoted as $P(z_s)$.

Photometric redshift uncertainties are one of most important systematic effects in weak lensing cosmology, and can cause significant biases in the cosmological parameters if they are affected by unknown residual systematic errors. To minimize the impact of such errors, we will adopt the method in Oguri and Takada [60] that allows one to self-consistently calibrate such photo- z errors, using a single sample of photometric source galaxies and multiple samples of spectroscopic lens galaxies in galaxy-galaxy weak lensing measurements.

For this purpose, we define a sample of background galaxies that satisfies

$$\int_{z_{l,\max}+z_{\text{diff}}}^7 P(z_s) dz_s \geq p_{\text{thresh}}, \quad (1)$$

where $z_{l,\max}$ was chosen to be equal to 0.70, the maximum redshift of the lens samples that we will use for the galaxy-galaxy lensing measurements (see below), $z_{\text{diff}} = 0.05$ and $p_{\text{thresh}} = 0.99$. Such cuts significantly reduce the contamination of source galaxies which are physically associated with the lens galaxies which can dilute the weak lensing signal at small separations. As our default choice, we use the $P(z)$ estimates for each galaxy provided by DEmPz.

The selection [Eq. (1)] reduces the total number of galaxies in our weak lensing sample to be just 24% of the original shape catalog [61], with an effective number density of 4.9 galaxies per square arcmin. Instead, if we use the posterior distributions of the redshifts given by DNNZ or Mizuki, the number of galaxies is 9% or 35% of the entirety of the shape catalog, respectively. These would correspond to an effective number density of 1.9 and 6.8 galaxies per square arcmin for DNNZ and Mizuki, respectively. These differences in the number density are entirely driven by the differences in the widths of the individual $P(z)$'s inferred by the different codes. The inferred $P(z)$ estimates for individual galaxies obtained using DNNZ are on average broader than those obtained in Mizuki and DEmPz. The broader widths result in a smaller number of galaxies that satisfy the cut shown in Eq. (1).

The inferred redshift distributions of the sample of our fiducial sources are shown in Fig. 2 based on the Bayesian Hierarchical Inference presented in Rau *et al.* [62]. These redshift distribution inferences (90% credible region shown in gray) use both the individual redshift probability distribution functions (PDFs) from photometric redshift estimation codes, as well as the measurements of clustering of the galaxies in our source sample, with that of red galaxies selected by the CAMIRA algorithm [63,64]. The 90% credible intervals on the redshift inference from each of these techniques individually are shown as the red shaded region and black points with errors, respectively. As mentioned before, we have multiple choices of photometric redshift estimates for our sample of galaxies. Even though we select galaxies using the DEmPz redshift PDFs, the same source galaxy sample also has redshift estimates

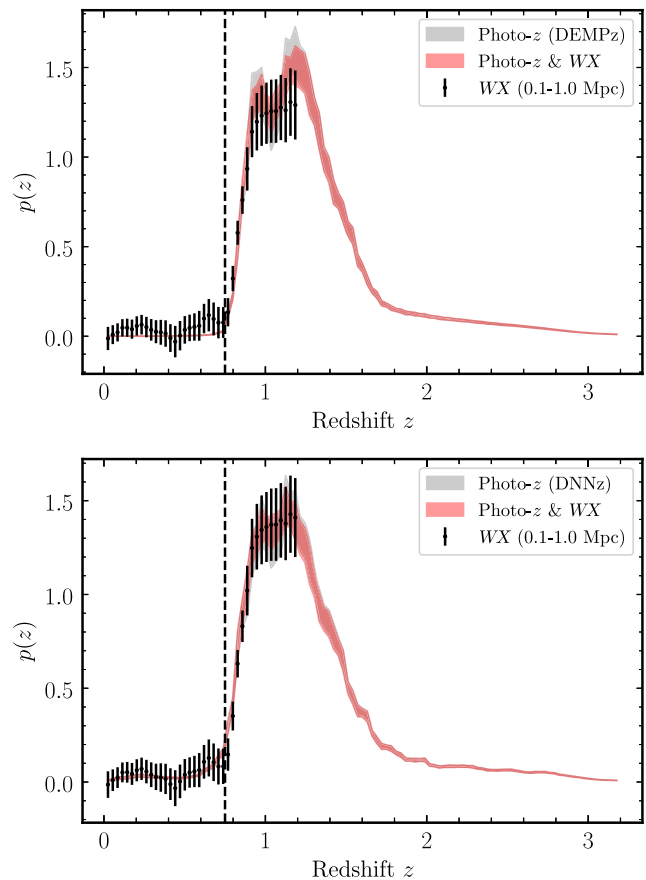


FIG. 2. The inferred redshift distribution of the source galaxies used in our weak lensing analysis obtained using the techniques described in [62]. The upper and lower panels use the photometric redshift PDFs for the source sample as inferred by the photo- z methods DEmPz and DNNZ, respectively. The gray shaded region shows the posterior based on deconvolving the photometric redshift errors from these PDFs, and the black points with errors correspond to the redshift inference based purely on the clustering of our source galaxies with the CAMIRA red galaxy sample, while the red shaded region corresponds to the posterior combining the two measurements.

characterized by the other codes, which help in pinning down any systematic uncertainties. The two panels in Fig. 2 correspond to the use of individual redshift PDFs from DEmPz and DNNZ, respectively, but for the same set of source galaxies. The clustering method does not extend to the entire range of redshifts as we run out of galaxies with well calibrated redshifts from CAMIRA beyond a redshift of 1.2. Note that the cross-correlation results (marked by WX) differ in each of the panels by their *a posteriori* normalization factor from the joint likelihood inference between WX and DNNZ/DEmPz, as can be seen upon a close inspection of the two panels. The redshift axes in each panel are aligned vertically for ease of comparison.

In the upper panel, we see a broad agreement between the redshift inference based on just the redshift PDFs from DEmPz and the clustering redshifts. However, it is interesting

to note that DEmPz predicts a bimodal feature in the redshift distribution with a dip in the number of galaxies with redshifts at $z \sim 1.0$. The clustering redshift inferences have large and correlated errors, but do not show any indication of such a bimodal distribution. The redshift inference based on DEmPz shows very small support at redshifts lower than 0.75 (less than 1%), by construction. In the bottom panel, which uses DNNZ estimates of the redshift PDFs, we do not see substantial evidence of a dip at redshift of unity in this inference. However, we notice that the inference using DNNZ does show some nonzero support even below the maximum lens redshifts we use of 0.75, as seen in the clustering measurements (although at low significance).

Any systematic differences in the redshifts of our sources could translate into biases in the measured weak lensing signals. In Appendix A, we present our estimates of such potential biases and suggest that shifting the inferred redshift PDFs by a free parameter Δz is sufficient in order to marginalize over such uncertainties with percent level accuracy.

B. Blinding strategy

All of our cosmological analyses are carried out in a two-tiered blind manner similar to our strategy in our Year 1 analysis [65]. As described in the HSC-Y3 shape catalog paper Li *et al.* [54], we use different multiplicative bias factors in order to blind our analyses in the first tier, which provide a convenient way to change the data vectors related to the weak lensing observables. We obtain three blind catalogs $i = 0, 1, 2$ where the j -th galaxy has a multiplicative bias equal to

$$m^{ij} = m^j + dm_1^i + dm_2^i, \quad (2)$$

where dm_1^i is a multiplicative bias known to the analysis lead designed to prevent unblinding due to accidental comparisons of multiple versions of the catalog. This value is removed in the measurement codes before performing any measurements with any of the catalogs. The three values dm_2^i are one of the three choices $(-0.1, -0.05, 0.)$, $(-0.05, 0., 0.05)$, $(0., 0.05, 0.1)$. These amplitude offsets are motivated by the differences in the values of amplitude of density fluctuations, σ_8 , as obtained by the CMB analysis by the Planck Collaboration [2] and other large-scale structure probes, e.g., [14,20]. All of our lensing related measurements were performed with all three blinded catalogs at the same time. The cosmological analyses and all systematic tests were performed on each of these catalogs, separately. As we will describe in Secs. VA and VIA in this paper, we modify our covariances to account for the fact that each of our catalogs has a different value of dm_2 (a procedure that can be performed without knowledge of dm_2). In this manner, the χ^2 of the best fit models to measurements performed using the three catalogs are not able to accidentally distinguish the true catalog.

The second tier of blinding is performed at the analysis level. The results of our analyses of all three catalogs prior to unblinding are presented by masking the value of the inferred cosmological parameters. Once all the analyses are performed and the relevant systematic checks are passed (see Paper II and III for a detailed checklist of tests to be passed prior to unblinding), we unblind each of the tiers, first starting with the second tier. The first tier of the catalog level unblinding is performed by a HSC team member external to the analysis team right at the end. Throughout this paper, we will show the measurements from our analysis of the blind catalog id = 2, which was found to be the true catalog post unblinding. No changes have been made to the analysis post unblinding. The other blinded catalogs also similarly passed each of the systematic tests as we show here for the blind catalog id 2.

C. Lens galaxy sample

We use the large-scale structure sample compiled as part of the Data Release 11 (DR11) [66,67] of the SDSS-III BOSS project [68] for measurements of the clustering of galaxies and as lens galaxies for the galaxy-galaxy weak lensing measurements. The lens galaxy sample used in this paper is the same as that used in the first year analysis of HSC data (Miyatake *et al.* [69], Sugiyama *et al.* [70]). The methodology used to construct the catalog is the same as that described in Miyatake *et al.* [71]. We briefly describe the catalog here.

The BOSS is a spectroscopic follow-up survey of galaxies and quasars selected from the imaging data obtained by the SDSS-I/II and covers an area of approximately 11,000 deg² [72] using the dedicated 2.5m SDSS Telescope [73]. Imaging data obtained in five photometric bands (*ugriz*) as part of the SDSS I/II surveys [74–76] were augmented with an additional 3,000 deg² in SDSS DR9 to cover a larger portion of the sky in the southern region [68,77–79]. These data were processed by a series of the photometric processing pipelines [80–82], and corrected for Galactic extinction [83] to obtain a reliable photometric catalog which serves as an input to select targets for spectroscopy [68]. The resulting spectra were processed by an automated pipeline to perform redshift determination and spectral classification [84]. The BOSS large-scale structure (LSS) samples are selected using algorithms focused on galaxies in different redshifts: $0.15 < z < 0.35$ (low redshift, LOWZ) and $0.43 < z < 0.70$ (constant mass, CMASS). In addition to the galaxies targeted by the BOSS project, these samples also include galaxies which pass the target selection but have already been observed as part of the SDSS-I/II project (legacy galaxies). These legacy galaxies were subsampled in each SDSS sector [85] of the sky so that they obey the same completeness as that of the LOWZ/CMASS targets in their respective redshift ranges [86].

Various color-magnitude selections guarantee a population of massive galaxies spanning a redshift range

$z \in [0.15, 0.70]$ in the spectroscopic survey. The resultant sample, however, is not entirely a volume or flux limited sample of galaxies.

The SDSS spectrograph can assign at most 1000 fibers on the sky at one time in a circular tile region (for the BOSS survey). Therefore an adaptive tiling algorithm was used to maximize the completeness of the survey. The spectra obtained from the observations were processed with SPECPIPE, the spectroscopic pipeline for determination of redshift and spectral classification. Despite all optimizations, there exist galaxies which obey the target selection, but cannot be assigned a fiber due to limitations of how close fibers can be assigned on a given tile. In such cases, the galaxy is assigned the redshift of its nearest neighbor galaxy which was assigned a fiber. A similar procedure is used to assign redshifts to galaxies for which SPECPIPE failed to determine a redshift. In the fiducial DR11 LSS catalog, the nearest neighboring galaxy gets an additional weight to account for the fiber-collided or redshift failure galaxy. We instead assign the nearest neighbor redshift to photometric galaxies with fiber collisions or redshift failures. This should be equivalent when the entire sample is used. However, our method allows for making further subsamples based on absolute magnitude. Guo *et al.* [87] have shown using detailed tests on mock galaxy catalogs that the nearest neighbor redshift correction achieves subpercent accuracy in the projected galaxy autocorrelation function for scales used in this paper.

This modified DR11 LSS sample described above forms our parent catalog. We obtain the $k + e$ -corrected i -band absolute magnitudes for individual SDSS galaxies using the k and e corrections tabulated in Wake *et al.* [88] relying on the “passive plus star-forming galaxies” spectral templates constructed using the stellar population synthesis model in Bruzual and Charlot [89] of individual galaxies based on $cmodel$ photometry. In order to minimize the effect of k corrections, we k correct the magnitudes of the LOWZ galaxies to a redshift of 0.20 and that of CMASS galaxies to a redshift of 0.55. As we will see below, these magnitudes allow us to define subsamples from this parent catalog.

We use weights provided for all galaxies to account for the inverse correlation between the number density of galaxies and that of stars [90], and that of seeing (w_*) as provided in the SDSS DR11 large scale structure catalogs [86].

We define three subsamples which are approximately volume limited by luminosity. The “LOWZ” subsample consists of galaxies with $z \in [0.15, 0.35]$, and the “CMASS1” and “CMASS2” subsamples consist of galaxies with $z \in [0.43, 0.55]$ and $z \in [0.55, 0.70]$, respectively. We apply further cuts on the absolute magnitude of galaxies of $M_i - 5 \log h < -21.5$, -21.9 and -22.2 for the three subsamples, respectively. This results in subsamples which have a number density equal to

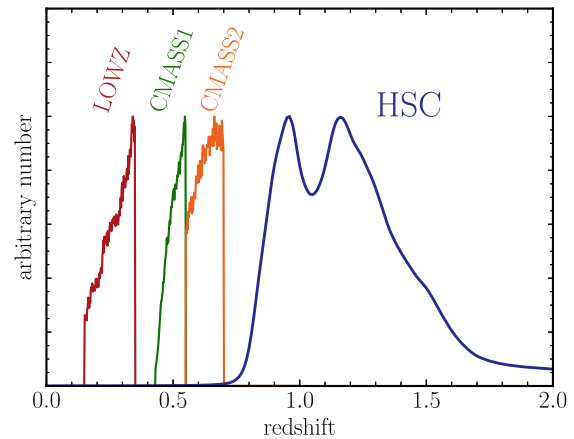


FIG. 3. The redshift distribution of the three spectroscopic lens samples are shown in red, green, and orange, respectively. These distributions can be compared to the redshift distribution of the HSC source galaxy sample used in our analysis shown in blue. In this figure the latter is estimated using stacked $P(z)$ distribution estimated by DEMpZ for the source galaxies used in our analysis.

$\bar{n}_g/[10^{-4}(h^{-1} \text{ Mpc})^{-3}] \simeq 1.8$, 0.74 and 0.45, respectively, which are a few times smaller than those of the entire parent (color-cut and flux-limited) LOWZ and CMASS samples. The redshift distribution of the three lens subsamples compared to the stacked $P(z)$ distribution for the HSC source galaxy sample we use in this paper is shown in Fig. 3 which shows the well separated redshift distributions of our lens subsamples compared to the source galaxies [91]. Please see Fig. 1 in Miyatake *et al.* [69] for the redshift distribution of the three luminosity-limited subsamples, compared to that of the flux-limited sample. As we will show in Secs. IV B and V B, use of such subsamples helps reduce systematics related to the variation of the measurements within each of the three redshift bins.

We will use random points in order to measure the galaxy clustering signal from these subsamples, as well as testing for systematics in the lensing signal. The random points are also useful to infer the potential dilution of the weak lensing signal due to the use of galaxies physically clustered with our subsamples, but are inferred to be at a higher redshift due to systematic and statistical errors in the photometric redshift distribution. The random points for each of our galaxy samples were constructed by downsampling the DR11 LSS random catalogs which follow the angular mask and redshift distributions of all galaxies in the LOWZ and CMASS samples, respectively, such that they follow the redshift distributions of our galaxy subsamples.

We will show that the clustering and lensing observables within the redshift bin of each sample do not evolve significantly given the approximate volume-limited nature of our catalogs, compared with that for the flux-limited sample. This is similar to the findings in Miyatake *et al.* [71], their Fig. 3], but for a sample of stellar mass selected

galaxies. Our samples also allow a simpler treatment of the magnification bias effect on the galaxy-galaxy weak lensing than the flux-limited sample; see [69,70].

D. Simulations for covariance measurements

In order to carry out the Bayesian inference of the cosmological parameters, we will compare the measurements of the galaxy clustering and galaxy-galaxy lensing signal of the lens subsamples described in the subsection above with theoretical models. The covariance matrix of these measurements provides a metric to compare the theoretical predictions to these observations, and thus a robust determination of uncertainties in the inferred parameters, which is a crucial component of a Bayesian analysis. We use mock catalogs of SDSS and HSC galaxies, generated from the N-body simulation based full-sky light-cone simulations [45], to estimate the covariance matrix for our observables; also see Appendix B of Ref. [69] for details. We produce a large number of synthetic SDSS galaxy mocks which are consistent with the measured clustering properties of SDSS galaxies. The HSC galaxy mocks also include properties of the galaxies such as the angular positions of each galaxy, their galaxy shapes and the simulated lensing effect. We perform mock measurements of galaxy clustering and galaxy-galaxy lensing signal with such synthetic galaxy data, in order to estimate the statistical uncertainties.

1. Generation of mock shape catalogs

We present the creation of the mock catalogs of galaxy shapes for the HSC-Y3 data. We use the 108 full-sky lensing simulations in Takahashi *et al.* [45] in order to construct the mock catalogs. These simulations adopt a flat Λ CDM cosmology consistent with the nine-year WMAP cosmology (WMAP9) [92]. To produce a set of galaxy shape catalogs, we follow the same methodology as adopted in Shirasaki *et al.* [93].

We use 13 different rotations of the HSC-Y3 sky area on the full sky to extract 13 approximately nonoverlapping HSC-Y3 survey footprints out of each full-sky lensing map. The full-sky lensing map yields the shear for a given source redshift at the location of each healpix pixel within the mock survey footprints. In total, we thus have $108 \times 13 = 1404$ realizations of shear in a number of lensing planes on a footprint equivalent to that of the HSC-Y3 data. These shear maps are then rotated back so that they occupy the same sky coordinates as the HSC-Y3 footprint.

We use these shear maps to construct mock shape catalogs by using the observed photometric redshifts and angular positions of real galaxies from the HSC-Y3 shape catalog. We rotate the shape of each source galaxy at random to erase the real lensing signal imprinted on the HSC galaxies. In practice, we first rotate the distortion of individual galaxies ϵ^{obs} and obtain the rotated distortion as $\epsilon^{\text{ran}} = \epsilon^{\text{obs}} e^{i\phi}$, where ϕ is a random number between 0 and

2π . We have to be careful that the observed distortion of a galaxy is different from the intrinsic distortion due to the measurement error. We model the intrinsic shape ϵ^{int} and measurement error ϵ^{mea} in the following manner:

$$\epsilon^{\text{int}} = \left(\frac{\epsilon_{\text{rms}}}{\sqrt{\epsilon_{\text{rms}}^2 + \sigma_e^2}} \right) \epsilon^{\text{ran}}, \quad (3)$$

$$\epsilon^{\text{mea}} = N_1 + iN_2, \quad (4)$$

where N_i is a random number drawn from a normal distribution with a standard deviation of σ_e . The first equation guarantees that the root-mean-squared (rms) ellipticity of the rotated intrinsic ellipticity is equal to ϵ_{rms} . We use ϵ_{rms} (parameter `i_shapehsmregauss_derived_rms_e`) and σ_e (parameter `i_shapehsmregauss_derived_sigma_e`) that are provided on an object-by-object basis in the HSC-Y3 shape catalog.

We draw a true redshift for the galaxy randomly from its individual photometric redshift PDF based on the photo- z code DNNZ. The choice for the use of DNNZ was due to the availability of the redshift PDF estimates at an early stage after the internal data release on which the shape catalog is based. We add the lensing shear on the source galaxy from the shear map on a lensing plane closest to the true redshift drawn for the galaxy thus assigning it an ellipticity given by

$$\epsilon_1^{\text{mock}} = \frac{\epsilon_1^{\text{int}} + \delta_1 + (\delta_2/\delta^2)[1 - (1 - \delta^2)^{1/2}](\delta_1\epsilon_2^{\text{int}} - \delta_2\epsilon_1^{\text{int}})}{1 + \delta \cdot \epsilon^{\text{int}}} + \epsilon_1^{\text{mea}}, \quad (5)$$

$$\epsilon_2^{\text{mock}} = \frac{\epsilon_2^{\text{int}} + \delta_2 + (\delta_1/\delta^2)[1 - (1 - \delta^2)^{1/2}](\delta_2\epsilon_1^{\text{int}} - \delta_1\epsilon_2^{\text{int}})}{1 + \delta \cdot \epsilon^{\text{int}}} + \epsilon_2^{\text{mea}}, \quad (6)$$

where $\delta \equiv 2(1 - \kappa)\gamma/[(1 - \kappa)^2 + \gamma^2]$ and κ and γ are simulated lensing convergence and shear at the galaxy position, taken from the ray-tracing simulation. Note $\delta \simeq 2\gamma$ in the weak lensing regime, and we do not include any multiplicative and additive biases in mock catalogs in Eqs. (5) and (6). Our method maintains the observed properties of the source galaxies on the sky including the lensing weights.

2. Generation of mock SDSS galaxy catalogs (lens and clustering samples)

We populate galaxies in the dark matter halos in each of our realizations using a halo occupation distribution (HOD) framework. The HOD $\langle N \rangle_M$ defines the number of galaxies in a halo of mass M . As is standard practice, we divide the HOD into a central and a satellite galaxy component, where

$$\langle N_{\text{gal}} \rangle_M = \langle N_{\text{cen}} \rangle_M + \langle N_{\text{sat}} \rangle_M, \quad (7)$$

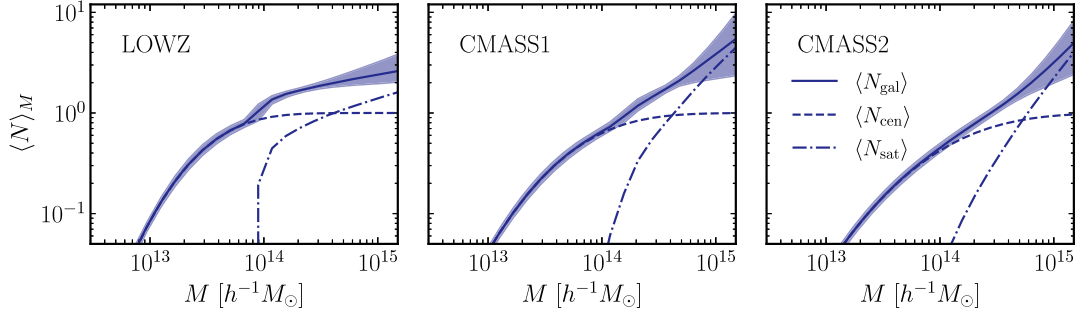


FIG. 4. The number of galaxies in a halo of mass M predicted by the HOD model with HOD parameters obtained from the emulator based model fitting to the clustering signal for each sample of the SDSS-BOSS galaxies. This HOD model is used to populate galaxies in mock simulations, which in turn are used to compute the covariance matrix of our observables.

with

$$\langle N_{\text{cen}} \rangle_M = \frac{1}{2} \left[1 + \text{erf} \left(\frac{\log_{10} M - \log_{10} M_{\text{min}}}{\sigma_{\log_{10} M}} \right) \right], \quad (8)$$

$$\langle N_{\text{sat}} \rangle_M = \langle N_{\text{cen}} \rangle_M \left(\frac{M - \kappa_M M_{\text{min}}}{M_1} \right)^{\alpha_M}. \quad (9)$$

To estimate HOD parameters, we first measure the clustering abundance of the LOWZ, CMASS1, and CMASS2 sample using the clustering measurement pipeline described in Sec. III A. The clustering covariance is obtained using 192 approximately equal area jackknife regions of the SDSS footprint. We also measure the abundance of each sample. To avoid an overdependence of the HOD constraints on the abundances, we use a more conservative 10% error estimate on these measurements. We model these measurements by emulator-based halo model [69] to obtain the HOD parameters, where we adopt the fitting range $0.5 < R/[h^{-1} \text{Mpc}] < 80$. Note that we assume WMAP9 flat- Λ CDM cosmology [92] for the

TABLE I. HOD parameters that best fit the clustering measurements for the three different subsamples along with the median redshift are noted in the different columns of the table. The mock galaxy catalogs are populated with these halo occupation distribution parameters. We provide the exact numbers we use for the population of the catalog; the number of significant digits mentioned are entirely for completeness and should not be taken to indicate the error on the determination of these HOD parameters.

	LOWZ	CMASS1	CMASS2
Median z	0.279	0.5206	0.6264
$\log M_{\text{min}}$	13.502510	13.835350	14.134250
σ^2	0.271474	0.473399	0.699328
$\log M_1$	14.435000	14.614390	14.686320
α	0.334696	1.868055	1.803775
κ	2.620329	0.017179	0.016590

measurements and fitting. The resultant halo occupation distribution fits are shown in Fig. 4, and the corresponding best fit parameters for the three subsamples are noted in Table I. Given that we are only using the clustering signal to fit the halo occupation distribution parameters, we expect a large number of degeneracies to be unresolved.

We use these parameters to populate galaxies in dark matter halos in the following manner. For every halo in the simulation, we compute the central halo occupation $\langle N_{\text{cen}} \rangle_M$, which acts as a probability for it to host a central galaxy within the halo. The central galaxy is assumed to reside at the center of each halo and is at rest with respect to its host halo. For halos which have central galaxies, we populate satellite galaxies with a Poisson deviate with mean $\lambda_M = [(M - \kappa_M M_{\text{min}})/M_1]^{\alpha_M}$. The satellite galaxies are assumed to have a radial distribution that follows the Navarro–Frenk–White profile [94] with a concentration parameter as measured by the halo finder ROCKSTAR [95]. The satellite galaxies are assigned a velocity with respect to the halo which is drawn from a Gaussian with zero mean and variance equal to $\sigma_{\text{vir}}^2 = (1+z)GM/(2R_{200\text{m}})$. The $(1+z)$ factor in this equation accounts for the fact that the halo radius is measured in comoving units.

III. MEASUREMENT CODES

In this section we describe the various analysis codes we use for carrying out the galaxy clustering, galaxy-galaxy lensing and the cosmic shear measurements as well as their covariances using the mock catalogs we have described in the previous section.

A. Clustering pipeline

The measurement of the clustering signal requires fast computation of pair counts at a variety of separations. We use a custom “clustering_pipeline” specifically developed for the measurement of weighted paircounts at a given projected separation R and line-of-sight separation π starting from catalogs of angular positions, redshifts and weights. The core functions of the pipeline are written in

C++, which are then exposed to python using the Simplified Wrapper and Interface Generator (SWIG).

The nearest neighbor searches are carried out with the help of a kd-tree [96] optimized to utilize the cache and enable fast searches for potential neighbors in the galaxy catalog in the plane of the sky. The value of R_{\max} and π_{\max} are used to leave out galaxy pairs that do not lie within the required projected and line-of-sight distances from each other.

The python functions allow input catalogs to be read in a variety of formats such as plain text, fits and csv files with information about the angular positions, redshifts, and weights of galaxies. These are then passed to the C++ code in order to generate the kd-tree for the paircounts. We use the Landy-Szalay estimator in order to measure the 3D correlation function,

$$\xi(R, \pi) = \frac{DD - 2DR + RR}{RR}. \quad (10)$$

where DD denotes the number of pairs of galaxies in the data, DR the number of normalized galaxy random pairs, and RR the number of normalized random random pairs at a given separation (R, π) . We use 50 times more randoms than the data points in order to reduce the shot noise in the determination of DR and RR .

The computation of the pair counts are done using the Message Passing Interface using a division of tasks for each of these pair counts. The load balancing is achieved by dividing the randoms into 50 separate units and computing the pair counts separately. The C++ code can also compute jackknife covariances on the fly if every galaxy is associated with a jackknife index.

We compute the three-dimensional correlation function $\xi(R, \pi)$ and integrate it along the line of sight direction to obtain the projected correlation function w_p ,

$$w_p(R) = 2 \int_0^{\pi_{\max}} \xi(R, \pi) d\pi. \quad (11)$$

We use $\pi_{\max} = 100h^{-1}$ Mpc. This length is smaller than the line-of-sight direction width of our subsamples and larger than the maximum projected distance to which we compute w_p .

The measurements of the clustering signal $w_p(R)$ are dependent upon the fiducial cosmological model used to compute these measurements. In the modeling analysis we account for the cosmology dependence of the measurements using the formalism presented in More *et al.* [37] during the modeling phase. Briefly, the fiducial cosmological model used to measure the clustering enters the measurements when the angular separations between the galaxies get converted into comoving separations and the redshift differences in to line-of-sight comoving separations. The ratio of the comoving distance to the

median redshift of each sample between the fiducial model and the cosmological model under consideration, as well as a similar ratio between the Hubble parameters in the two models can correct for the clustering measurements. On the other hand, for the weak lensing signal, we additionally have to consider the dependence of the critical surface density on the fiducial cosmological parameters and the cosmological model under consideration.

The various inputs to the clustering pipeline such as the cosmological model to be used for the measurements, the minimum and maximum projected distances, the number of radial bins, the number of bins in projected radius, the types of galaxies used to measure the clustering (cross or auto) are passed via a simple yaml file.

The pipeline has been validated by comparing the correlation function measurements against those measured by the BOSS survey collaboration using the entire BOSS-LOWZ and BOSS-CMASS samples.

B. Galaxy-galaxy lensing pipeline

The gravitational lensing owing to the presence of mass between us and the far away source galaxies results in coherent distortions in their shapes. Such distortions can be inferred from the observed distribution of ellipticities of these galaxies. As galaxies have intrinsic shapes, this signal needs to be measured as a statistical average of the shapes of a large number of galaxies.

The HSC-Y3 shape catalog provides the ellipticity components (e_1, e_2) along with the weights for every galaxy w_s , the additive and multiplicative biases (c_1, c_2, m) and the variance of the ellipticity e_{RMS} . Given ϕ , the angle between the line joining the lens and the source galaxy in the plane of the sky and the x axis of the coordinate system, the tangential distortion in shape is given by

$$e_t = -e_1 \cos(2\phi) - e_2 \sin(2\phi). \quad (12)$$

The average of the tangential ellipticity is proportional to the tangential shear induced on the galaxy by the matter distribution correlated with the lens galaxy. The tangential shear depends upon the surface mass density, $\Sigma(R)$, and the critical surface density for lensing Σ_{crit} such that

$$\gamma_t(R) = \frac{\Sigma(< R) - \Sigma(R)}{\Sigma_{\text{cr}}(z_l, z_s)} = \frac{\Delta\Sigma(R)}{\Sigma_{\text{cr}}(z_l, z_s)}. \quad (13)$$

Here, the symbol $\Sigma(< R)$ denotes the average surface mass density within a projected distance R from the lens, and $\Sigma(R)$ is the surface mass density at the distance R after performing an azimuthal average. The critical surface density, $\Sigma_{\text{cr}}(z_l, z_s)$, is a geometrical factor dependent on the angular diameter distances to the lens $D_A(z_l)$, the source $D_A(z_s)$ and between the two, $D_A(z_l, z_s)$. When expressed in comoving units, the critical surface density is given by

$$\Sigma_{\text{cr}}(z_1, z_s) = \frac{c^2}{4\pi G} \frac{D_A(z_s)}{D_A(z_1)D_A(z_1, z_s)(1+z_1^2)}. \quad (14)$$

As the galaxy-galaxy lensing signal, we measure the excess surface density $\Delta\Sigma(R) = \Sigma(<R) - \Sigma(R)$ as a minimum variance weighted statistical average,

$$\Delta\Sigma(R) = \frac{1}{(1+\hat{m})} \left(\frac{\sum_{\text{ls}} w_{\text{ls}} e_{t,\text{ls}} \langle \Sigma_{\text{cr}}^{-1} \rangle_{\text{ls}}^{-1}}{2\mathcal{R} \sum_{\text{ls}} w_{\text{ls}}} \right). \quad (15)$$

The average inverse critical surface density is computed from the full photometric redshift posterior distribution, $p(z_s)$,

$$\langle \Sigma_{\text{cr}}^{-1} \rangle_{\text{ls}} = \frac{4\pi G(1+z_1)^2}{c^2} \int_{z_1}^{\infty} \frac{D_A(z_1)D_A(z_1, z_s)}{D_A(z_s)} p(z_s) dz_s, \quad (16)$$

where the lower limit of the integration is from the lens redshift z_1 . Given the photometric redshift errors, one can expect galaxies in the foreground or at the lens redshifts to be in our source sample. To reduce the effects of such galaxies we only choose those sources that have a large probability to lie at a specified redshift according to Eq. (1). The parameter z_{max} can be chosen to correspond to the maximum redshifts of the sample, and the tunable parameters z_{diff} and p_{cut} which can be changed to allow the cuts to be more stringent. Alternatively, the pipeline also allows for the possibility to carry out the source selection by using the best estimate of the photometric redshift.

The weight used in Eq. (15), $w_{\text{ls}} = w_1 w_s \langle \Sigma_{\text{cr}}^{-1} \rangle_{\text{ls}}^2$, is the minimum variance weight for the estimator of the signal $\Delta\Sigma$, and it down weights those lens-source pairs that are close to each other in redshift. The shear responsivity \mathcal{R} is given by

$$\mathcal{R} = 1 - \frac{\sum_{\text{ls}} w_{\text{ls}} e_{\text{RMS}}^2}{\sum_{\text{ls}} w_{\text{ls}}}, \quad (17)$$

and can be estimated from e_{RMS} . Finally, the term \hat{m} is the average multiplicative bias and is defined as $\hat{m} = \sum_{\text{ls}} w_{\text{ls}} m_s / \sum_{\text{ls}} w_{\text{ls}}$.

In addition, we consider the effect on the multiplicative and the additive selection bias. Li *et al.* [54] found that the multiplicative bias and selection bias are proportional to the fraction of galaxies at the sharp boundary of selection cuts on resolution and aperture magnitude as follows:

$$\hat{m}_{\text{sel}} = -0.05854 \hat{P}(\text{mag}_A = 25.5) + 0.01919 \hat{P}(R_2 = 0.3), \quad (18)$$

$$\hat{a}_{\text{sel}} = 0.00635 \hat{P}(\text{mag}_A = 25.5) + 0.00627 \hat{P}(R_2 = 0.3), \quad (19)$$

respectively. Here, $\hat{P}(X)$ is the fraction estimate of galaxies at the boundary of selection cut on X . The galaxy-galaxy lensing estimate is corrected as

$$\Delta\Sigma \rightarrow \frac{1}{1+\hat{m}_{\text{sel}}} (\Delta\Sigma - \hat{a}_{\text{sel}} \Delta\Sigma^{\text{psf}}), \quad (20)$$

$$\Delta\Sigma^{\text{psf}} = \frac{\sum_{\text{ls}} w_{\text{ls}} e_{t,\text{ls}}^{\text{psf}}}{\sum_{\text{ls}} w_{\text{ls}}}, \quad (21)$$

where e_i^{psf} is the PSF shape.

Finally we also repeat the same exact measurement procedure mentioned above for the weak lensing signal but around random points which are 40 times larger than the number of lenses. We use random catalogs which occupy the same area on the sky and follow the same redshift distributions as our lens subsamples. This allows us to subtract out any large-scale systematic effects that may exist, especially on scales comparable to the field of view of HSC. This changes our final estimator from the one written in Eq. (20),

$$\Delta\Sigma \rightarrow \Delta\Sigma - \Delta\Sigma_{\text{rand}}. \quad (22)$$

The weak lensing pipeline we have developed implements the above calculations in order to measure the galaxy-galaxy lensing signal. At its core, it needs to perform nearest neighbor calculations on the plane of the sky between lens and source galaxies. It uses the same kd-tree code as used in the galaxy clustering pipeline in order to speed up these calculations. The core functions of the pipeline are again written in C++ for speed, with interfaces provided via python using SWIG. The input and output is handled on the python side making it easier to swap in and out different catalogs for the lensing measurements while preserving the core functionality.

In order to make the code memory efficient, we search for lens galaxies around source galaxies rather than the other way around. The computational complexity of the algorithm to generate a tree of N points and to perform n searches with it is $\mathcal{O}[(N+n)\log N]$; thus it is better to generate the tree out of the smaller of the two numbers. Given the order of magnitude difference between the number of galaxies in the lens and the source samples, we generate the tree using the lens catalogs. This in turn also makes the code memory efficient, because the entirety of the source catalog need not be read right at the beginning in order to generate the tree.

The computation of the weak lensing signal and the covariance is parallelized using a division of tasks. Given that the code requires one to compute the weak lensing signal around random points, we usually divide the task into computation of the weak lensing signal around the lens galaxy samples and the randoms into separate tasks. The

covariance computations are also performed by running the weak lensing pipeline over a large number of mock catalogs. This allows us to massively parallelize the computation of the weak lensing signal and covariances. The code also allows for the computation of the weak lensing signal in different fields separately. The output of the weak lensing pipeline has all the relevant outputs which can then later be combined in the postprocessing.

The various inputs to the weak lensing pipeline such as the cosmological model to be used for the measurements, the minimum and maximum projected distances, the number of radial bins, the lens and source selection parameters can all be passed via simple yaml files. The pipeline has been validated by comparing the weak lensing measurements with a number of independent codes written by other authors in the HSC survey collaboration.

C. Cosmic shear measurement code

In order to compute the cosmic shear, we use the estimator in Li *et al.* [54] for the shear estimate for each galaxy,

$$\hat{\gamma}_i = \frac{1}{(1 + \hat{m})} \left[\frac{e_i}{2\mathcal{R}} - c_i \right]. \quad (23)$$

In this case the weighted average multiplicative bias factor is given by

$$\hat{m} = \frac{\sum_i w_i m_i}{\sum_i w_i}, \quad (24)$$

and the weight in this equation corresponds to the shape weight w_s given in the HSC shape catalog [54]. The shear responsivity in this case is estimated using

$$\mathcal{R} = 1 - \frac{\sum_i w_i e_{\text{rms},i}^2}{\sum_i w_i}. \quad (25)$$

As in the galaxy-galaxy lensing measurement, we take account of the multiplicative and the additive selection biases in the cosmic shear measurement

$$\hat{\gamma}_i \rightarrow \frac{1}{1 + m_{\text{sel}}} (\hat{\gamma}_i - a_{\text{sel}} e_i^{\text{psf}}), \quad (26)$$

where m_{sel} and a_{sel} are evaluated using the entire sample of our source galaxies.

We use the software `TreeCorr`, in order to compute the two-point shear correlation functions ξ_+ and ξ_- . In our case we use a single source sample which would allow us to self-calibrate any residual uncertainties in the determination of the true redshift distribution given the photometric redshifts of our galaxies. We estimate ξ_{\pm} as

$$\xi_{\pm}(\theta) = \frac{\sum_{ij} w_i w_j [\hat{\gamma}_{i,i} \hat{\gamma}_{j,t} \pm \hat{\gamma}_{i,x} \hat{\gamma}_{j,x}]}{\sum_{ij} w_i w_j}, \quad (27)$$

and the summation runs over all pairs of galaxies i, j whose angular separation falls within a bin of given width around θ .

We also diagnose any contamination of the above correlations due to the presence of PSF anisotropies. Such residuals are expected to be present due to the imperfections in the modeling and the measurements of the PSF. We continue to follow the prescription presented in Hikage *et al.* [97] and Troxel *et al.* [98], such that the systematics due to the PSF errors are added in a linear fashion and arise from two sources,

$$\gamma^{\text{sys}} = \alpha_{\text{psf}} \gamma^{\text{p}} + \beta_{\text{psf}} \gamma^{\text{q}}, \quad (28)$$

where γ^{p} is the shape of the PSF model, and γ^{q} is the difference between the true PSF of stars and the model PSF at their locations. These two terms account for the error in the deconvolution of the PSF from the galaxy shapes and the error in the shapes due to the imperfect modeling of the PSF. These terms give rise to a spurious component in the measured cosmic shear signal, ξ_{psf} given by

$$\hat{\xi}_{\text{psf},\pm}(\theta) = \alpha_{\text{psf}}^2 \xi_{\pm}^{\text{pp}} + 2\alpha_{\text{psf}} \beta_{\text{psf}} \xi_{\pm}^{\text{pq}} + \beta_{\text{psf}}^2 \xi_{\pm}^{\text{qq}}. \quad (29)$$

Here the quantities ξ_{\pm}^{pp} and ξ_{\pm}^{qq} are the autocorrelations of γ^{p} and γ^{q} , respectively, and ξ_{\pm}^{pq} corresponds to the cross-correlation of the two quantities. These correlations can be measured directly from the data by using the shapes of stars, that were reserved for modeling the PSF over the entire field of view. In HSC, the PSF measurement and modeling are performed over each exposure, rather than the coadd, and 20% of the stars are randomly reserved for PSF testing. Since these stars are randomly selected during each exposure, the number of stars that are never used in the PSF determination is quite small. The HSC pipeline assigns a flag `i_calib_psf_used` to denote stars that have been used for the PSF determination at least in 80% of the visits they belong to. We use stars with flags `I_CALIB_PSF_USED i_calib_psf_used=True` to compute these correlations, because it is less noisy. We also take into account the uncertainty of the predicted $\hat{\xi}_{\text{psf},\pm}$ whether we use `I_CALIB_PSF_USED i_calib_psf_used=True` or `False`. In Sec. VI B, we will present our constraints on the parameters α_{PSF} and β_{PSF} and our suggested priors for the cosmological analyses.

Note that our treatment of the PSF systematics in the 3×2 pt analyses differs from the default setup used in the cosmic shear analyses alone in our companion papers Li *et al.* [43] and Dalal *et al.* [44], where we account for the errors in the PSF moments up to fourth order following the methodology developed in [99]. In Sugiyama *et al.* [42] and

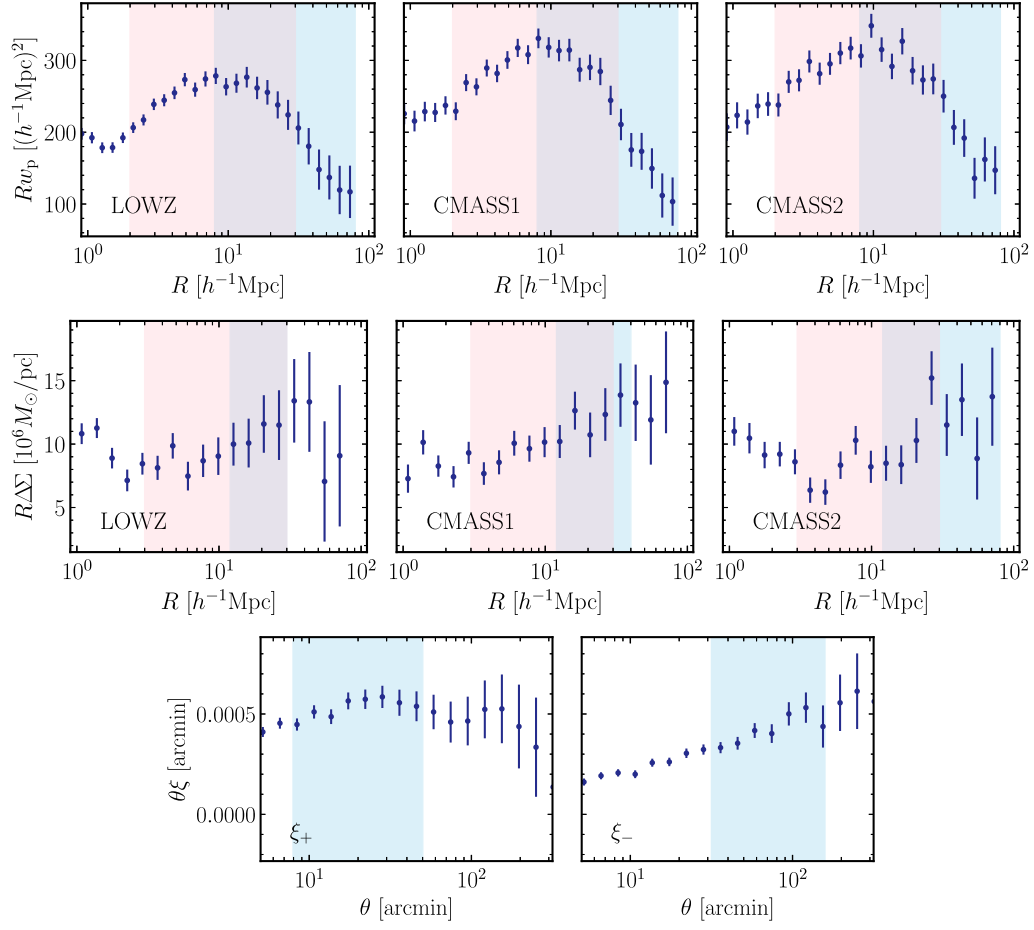


FIG. 5. The measurements of the 3×2 pt functions that will be used for the cosmology parameter inference in companion papers, Miyatake *et al.* and Sugiyama *et al.* Top panels: the clustering signals of spectroscopic SDSS galaxies are shown for LOWZ, CMASS1 and CMASS2 in redshift bin $z \in [0.15, 0.35]$, $[0.43, 0.55]$ and $[0.55, 0.70]$ from left to right panels, respectively. Although the signal is identical to the Year 1 analysis [18,70], the updated covariance is measured from mock catalogs described in this paper. The shaded regions indicate the scales used for cosmology analyses in the companion papers: blue for the large-scale analysis with minimal bias model by Sugiyama *et al.*, and red for the small-scale analysis by Miyatake *et al.* Middle panels: the galaxy-galaxy weak lensing signals measured by combining the spectroscopic SDSS galaxies and HSC-Y3 source galaxies. For the measurement of clustering and galaxy-galaxy lensing signals, we used a flat Λ CDM model with $\Omega_m = 0.279$ to convert angular separation θ to physical separation R and to compute $\langle \Sigma_{\text{cr}} \rangle$. Bottom panels: the cosmic shear correlation functions for the plus and minus modes are shown in the left and the right panels, respectively. The blue shaded regions indicate the scales used for both of the large-scale and the small-scale cosmology analyses.

Miyatake *et al.* [41], we will test the impact of including such an effect for the HSC source galaxies used in our analyses and quantify its impact on the cosmological parameters.

Finally, we also will perform an E/B mode decomposition of the measured cosmic shear two-point correlation functions, such that

$$\xi_E(\theta) = \frac{\xi_+(\theta) + \xi'(\theta)}{2}, \quad (30)$$

$$\xi_B(\theta) = \frac{\xi_+(\theta) - \xi'(\theta)}{2}, \quad (31)$$

where ξ' is given by

$$\xi'(\theta) = \xi_-(\theta) + 4 \int_{\theta}^{\infty} \frac{d\theta'}{\theta'} \xi_-(\theta') - 12\theta^2 \int_{\theta}^{\infty} \frac{d\theta'}{\theta'^3} \xi_-(\theta'). \quad (32)$$

We replace the integral with a Riemann sum over the range $\theta' \in [2, 420]$ and with logarithmic bins of size $\Delta \log \theta = 0.0222$. A larger bin size would smooth out the angle dependence of ξ_- , and affect the accuracy of the Riemann sum as a consequence. Therefore, we use narrower bins in θ for the measurement of ξ_{\pm} , decompose them into E/B modes using the above equations and then finally smooth the signal to obtain E/B signals over similar bins as the cosmology analysis. We have carefully checked that the results converge with the choice of the bins we use.

IV. CLUSTERING MEASUREMENTS

A. Measurements

We show the clustering signals we measure for the three subsamples in the three different panels of Fig. 5, respectively. Although we have measured the signals on small scales, we restrict to scales beyond $1h^{-1}$ Mpc. The measured projected correlation functions fall off approximately as $1/R$. The deviation from this power law can be seen clearly when we plot $w_p R$.

The clustering of LOWZ galaxies clearly shows the transition between the one-halo term and the two-halo term on scales around $1.5h^{-1}$ Mpc. This transition is less pronounced for the CMASS1 and CMASS2 subsamples. In both our cosmological analyses we avoid modeling below the transition scale due to uncertainties in the accuracy of their modeling. We have tested the accuracy of both of our modeling schemes against different systematic uncertainties and decided on the scale cuts that we will use for our analysis in Miyatake *et al.* [41] and Sugiyama *et al.* [42]. The validation of the scale cuts include tests on different models for how satellite galaxies populate dark matter halos, whether the central galaxies are off centered within their respective halos, the presence of incompleteness in the halo occupation distribution of central galaxies, or that of halo assembly bias, in addition to the choice of halo definitions in simulations. Based on the validation analyses, we use a range of $[2, 30]h^{-1}$ Mpc and $[8, 80]h^{-1}$ Mpc for the small-scale and large-scale analyses, respectively.

We use the 108 realizations of the full-sky mock catalogs imprinted with the BOSS LOWZ, CMASS1 and CMASS2

footprints. Within each realization we utilize 192 jackknife regions of the SDSS survey footprint (see [71] for details), measure w_p for each jackknife region, and estimate the covariance matrix from the measured w_p 's from all the jackknife regions. We then average the covariances for the 108 realizations to estimate the covariance matrix for each of the LOWZ, CMASS1, and CMASS2 subsamples. The covariance matrix estimated in this way is used for our cosmology analysis. Since the covariance matrix of w_p is estimated effectively from a larger number of samples $20,736 = (108 \times 192)$, the Hartlap factor [100] can be ignored in evaluating the inverse of the covariance matrix for the clustering sector. This is different from our analysis with Y1 data, where we just used the jackknife estimate of the covariance from the real data. Our new method allows the determination of the covariance with reduced noise properties.

One can also expect some cross covariance between the measurements as the CMASS1 and CMASS2 subsamples share a boundary and the galaxies near the boundary will share the same large-scale structure, although we expect this to be a small effect. Finally, we have also analytically checked that the magnification bias effect on the observed galaxy number density by gravitational lensing by foreground matter fluctuation has a negligible effect on the clustering covariance; thus we do not include the cross covariance between w_p 's for different subsamples.

The cross-correlation coefficients of the covariance result are shown in Figs. 5 and 6. The error bars in Fig. 5 show the diagonal elements of estimate covariance. Figure 6 shows the correlation coefficients of the

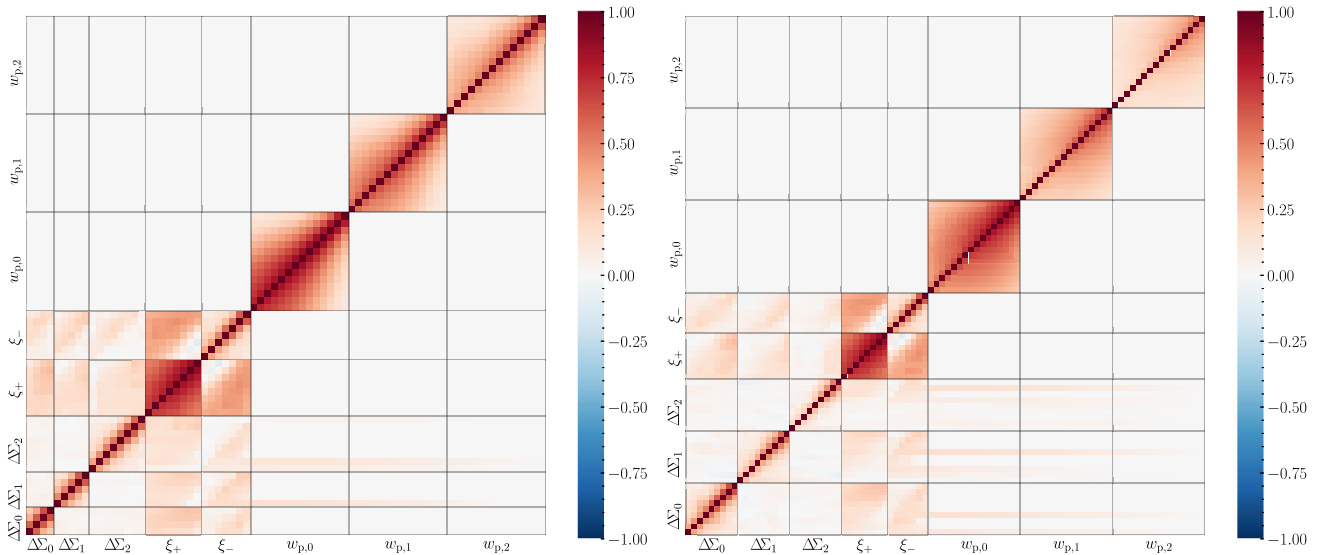


FIG. 6. The correlation coefficient of the full covariance matrix. Left: the large-scale cosmology analysis with minimal bias model. The scales shown in this figure are indicated by the shaded regions in Fig. 5. Subscripts of 0, 1, and 2 for $\Delta\Sigma$ and w_p stand for the LOWZ, CMASS1 and CMASS2 subsamples, respectively. The contribution of magnification bias is evaluated analytically and added on the covariance estimated from mock measurements. Right: similar to the left panel, but for the small-scale analysis.

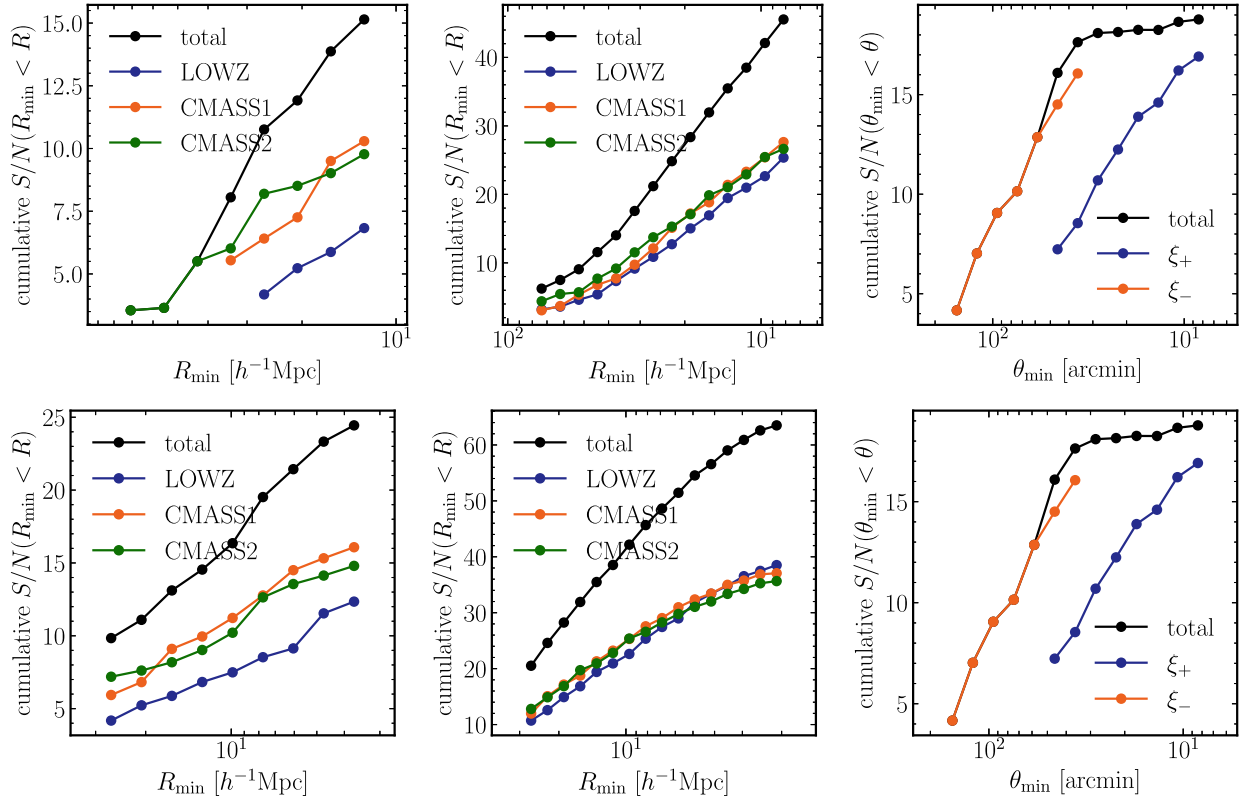


FIG. 7. The cumulative signal-to-noise ratios as a function of minimum scale cuts for clustering, galaxy-galaxy lensing and cosmic shear are shown in the different columns, respectively. The top and the bottom panels show the cumulative signal-to-noise ratio for large- and small-scale analysis respectively.

covariance, over the scale used for cosmology analyses: the large-scale analysis with minimal bias model by Sugiyama *et al.*, and red for the small-scale analysis with the emulator-based halo model by Miyatake *et al.*, respectively.

Figure 7 shows the cumulative signal-to-noise ratio as the function of minimum scale cut. The upper and lower panels are for large- and small-scale analysis, respectively. The total signal-to-noise ratios of our measurements in the LOWZ, CMASS1 and CMASS2 subsamples are 25.6, 27.6, 26.6, respectively for our large-scale analysis. When including the scales that will be modeled in our small-scale analysis, these signal-to-noise ratios increase to 38.5, 37.1, 35.7, respectively.

B. Systematic tests

We carry out a couple of tests in order to understand the possible systematics in our analysis. The first is the dependence of the galaxy number density in our lens sample on seeing and the number density of stars. In Ross *et al.* [4], these relations were calibrated based on the entire large-scale structure sample. Since we are including a cut on the luminosity which is dependent on luminosity we are preferentially selecting the brighter galaxies. If the dependence is weaker for brighter galaxies then we may end up giving extra weight to brighter galaxies.

To account for the reduction in the number density of galaxies in regions where there is a large stellar number density, the large-scale structure catalogs have been assigned a stellar density weight. Since this weight is also dependent on the magnitude of galaxies, we carry over the weights assigned to these galaxies even in our subsamples. In order to test how such systematic stellar weights affect the clustering signal, we show the variation of the clustering signal with and without the systematic star weights in Fig. 8. The effects on the clustering signal all appear within the statistical error budgets, especially considering the fact that the measurements are correlated on large scales.

Next, we also test out how much the clustering signal varies as a function of redshift. In our cosmological analyses we will consider the average redshift of each of the subsamples as the representative redshift for our measurements and compare it to the theoretical predictions for cosmological inference. The cosmological ingredients such as the halo mass function, the halo bias, and the clustering of matter with itself and the halos vary as a function of redshift. At fixed halo occupation distribution, these changes are at the subpercent level. Further, we also expect the clustering signal to vary with redshift if the halo occupation distribution of galaxies changes as a function of redshift.

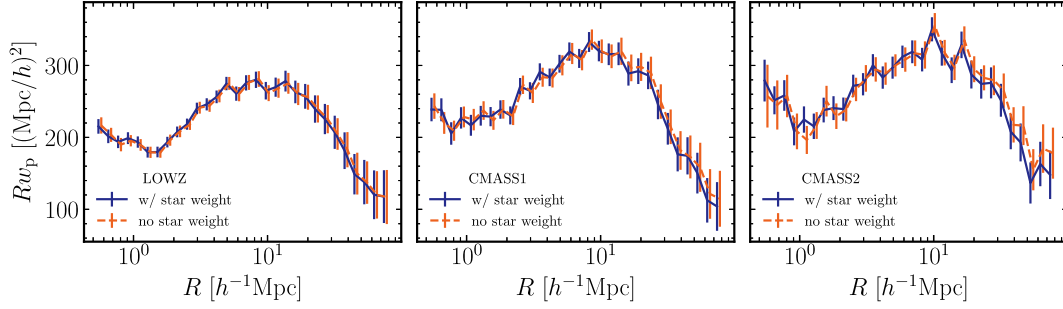


FIG. 8. The dependence of the clustering signals on the systematic weights related to seeing and stellar number density. We find a very weak dependence of these measurements on such systematic weights within the statistical errors.

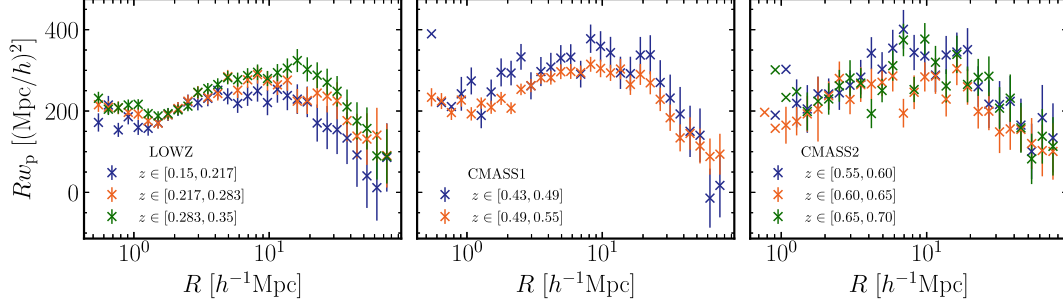


FIG. 9. The variation of the clustering signal within each lens redshift bin. Here, we divide the lens galaxy samples into two or three subsamples in each redshift bin. This should be compared with Fig. 20, where the BOSS full sample, i.e the flux-limited sample, is used for w_p measurement rather than the luminosity-limited samples presented in this paper.

We divide each of the LOWZ, CMASS1 and CMASS2 subsamples into three bins each and remeasure the clustering signal. We show the variation of the clustering signal as a function of redshift for the subsamples in each of the subpanels of Fig. 9. To assess the variation of the clustering amplitudes of the signal in each of the bins, we fit the signal with a fiducial model with our fiducial cosmological parameters at the median redshift of the sample with a free amplitude parametrized as

$$A(z) = A_0 + \alpha(z - z_{\text{med}}). \quad (33)$$

TABLE II. The slope of the systematic variation of the clustering signal with redshift for each of the subsamples and the small- and large-scale analyses are presented in the top and bottom sections, respectively. We find no significant evidence of variation with redshift.

Analysis	Sample	α
Small scale	LOWZ	0.0 ± 0.5
	CMASS1	-2.5 ± 1.4
	CMASS2	-1.1 ± 0.8
Large scale	LOWZ	0.2 ± 0.7
	CMASS1	-2.7 ± 1.8
	CMASS2	-0.6 ± 1.1

When we fit the clustering measurements on the large or small scales we obtain values of α all consistent within $2\text{-}\sigma$ (see Table II). This shows that the clustering signal does not show an appreciable variation with redshift.

V. LENSING MEASUREMENTS

We use the weak lensing pipeline described in Sec. III B in order to measure the galaxy-galaxy lensing signal around the three subsamples of lenses that we consider. In this section, we present these lensing measurements as well as our estimates of the covariance of these measurements using the mock catalogs.

We measure $\Delta\Sigma$ in 30 logarithmic radial bins in projected distance in the range $[0.05, 80.0]h^{-1}$ Mpc. As described before, we use the source catalog of HSC galaxies satisfying Eq. (1) with $z_{\text{min}} = 0.7, z_{\text{diff}} = 0.05, p_{\text{cut}} = 0.99$. We carry out our measurements of the weak lensing signal in the six different fields separately and later on combine them in postprocessing.

The measurement of the galaxy-galaxy lensing signal includes the conversion of galaxy shear γ_t to the matter surface density $\Delta\Sigma$ and the conversion of the angular radial bin θ to the projected radial bin R . To do these conversion, we assume a fiducial cosmology for measurement. Because we use the radial bin in the unit of h^{-1} Mpc and it is independent to the value of Hubble parameter h , the only relevant cosmological parameter is the matter density

parameter Ω_m in the flat Λ CDM model that we focus on in the companion cosmology papers. We use a flat Λ CDM model with $\Omega_m = 0.279$ as the fiducial cosmology for measurement.

A. Measurements and covariance

We show the weak lensing signal $\Delta\Sigma$ for the three subsamples used in our analysis in the three different panels in the middle row of Fig. 5, respectively. Although we have measured the signals on small scales, we restrict to scales beyond $1h^{-1}$ Mpc in our figure. The measured weak lensing signal falls off approximately as $1/R$. In the figure, we plot the quantity $R \times \Delta\Sigma$ as this shows the deviations from such a power law. In general we see similar amplitudes for the weak lensing signals across the three different subsamples.

For the covariance estimation, we measure the galaxy-galaxy lensing signals using mock lens galaxy catalogs described in Sec. II D 2 and the corresponding 1404 mock shape catalogs in Sec. II D 1. We construct a total data vector $\Delta\Sigma$ by concatenating the measurements of all three of our subsamples together. We obtain the covariance between these measurements as

$$C_{ij} = \langle (\Delta\Sigma_i - \overline{\Delta\Sigma}_i)(\Delta\Sigma_j - \overline{\Delta\Sigma}_j) \rangle. \quad (34)$$

Our blinding scheme described in detail in Sec. II B relies on the use of different multiplicative bias factors for three different catalogs, only one of which is correct. However, our mock simulations do not include any multiplicative bias factors. The covariance for the galaxy-galaxy lensing measurements computed in this manner cannot therefore be directly used with the three different blind catalogs.

To estimate the covariance for each of the blinded catalogs with nonzero multiplicative biases, we include the multiplicative bias in Eqs. (5) and (6) by changing $\gamma \rightarrow (1 + \hat{m})(1 + \hat{m}_{\text{sel}})\gamma$ at the catalog level. The value of the multiplicative bias \hat{m} is taken from the corresponding blind catalog. However, we have three different blind catalogs with different multiplicative bias, and iterating mock measurements for all the blind catalogs is computationally expensive. To avoid this iteration, we develop a rescaling method in order to obtain the galaxy-galaxy lensing signal with nonzero multiplicative bias from one without multiplicative bias. We first note that the observed galaxy ellipticity in Eqs. (5) and (6) in the presence of multiplicative biases can be expanded as

$$\mathbf{e}^{\text{mock}} = 2\mathcal{R}(1 + \hat{m})(1 + \hat{m}_{\text{sel}})\boldsymbol{\gamma} + \boldsymbol{\epsilon}^n, \quad (35)$$

to the lowest order of the intrinsic shape and the lensing shear, where $\boldsymbol{\epsilon}^n = \boldsymbol{\epsilon}^{\text{int}} + \boldsymbol{\epsilon}^{\text{meas}}$. Using this expansion, the estimator in Eqs. (15) and (20) is

$$\hat{\Delta\Sigma}(\hat{m}) \sim \hat{\Delta\Sigma}^{\text{sim}} + \frac{1}{(1 + \hat{m})} \frac{\sum_{\text{ls}} w_{\text{ls}} \epsilon_{t,\text{ls}}^n \langle \Sigma_{\text{cr}}^{-1} \rangle^{-1}}{(1 + \hat{m}_{\text{sel}}) 2\mathcal{R} \sum_{\text{ls}} w_{\text{ls}}}, \quad (36)$$

where the first term is

$$\hat{\Delta\Sigma}^{\text{sim}} = \frac{\sum_{\text{ls}} w_{\text{ls}} \gamma_{t,\text{ls}} \langle \Sigma_{\text{cr}}^{-1} \rangle^{-1}}{\sum_{\text{ls}} w_{\text{ls}}} - \frac{\hat{a}_{\text{sel}}}{1 + \hat{m}_{\text{sel}}} \Delta\Sigma^{\text{psf}}, \quad (37)$$

and $\epsilon_{t,\text{ls}}^{\text{int}}$, $\epsilon_{t,\text{ls}}^{\text{meas}}$, and $\gamma_{t,\text{ls}}$ are defined similarly as in Eq. (12) but with $\mathbf{e} \rightarrow \boldsymbol{\epsilon}^{\text{int}}$, $\boldsymbol{\epsilon}^{\text{meas}}$, and $\boldsymbol{\gamma}$. Note that $\hat{\Delta\Sigma}^{\text{sim}}$ can be measured from the mock catalog because we know $\boldsymbol{\gamma}$, but this is an unknown in the real measurement. The measurement of $\hat{\Delta\Sigma}^{\text{sim}}$ can be done at the same time by using the same lens-source pair stacking as $\hat{\Delta\Sigma}$, and does not require additional measurement. Using the dependence of $\hat{\Delta\Sigma}(\hat{m})$ on \hat{m} in Eq. (36), we obtain an equation for rescaling the $\Delta\Sigma$ measurements in the presence of multiplicative bias,

$$\hat{\Delta\Sigma}(\hat{m}) = \hat{\Delta\Sigma}^{\text{sim}} + \frac{\hat{\Delta\Sigma}(m=0) - \hat{\Delta\Sigma}^{\text{sim}}}{1 + \hat{m}}. \quad (38)$$

This method relies on the expansion of the estimator with respect to the intrinsic shape and the lensing shear in Eq. (36), which may lead to inaccuracy in the covariance estimate. We have checked that the rescaling method works at the 1% level in the covariance amplitude, by using 100 mock measurements and comparing the measurements made without the multiplicative bias but corrected using our formalism to those made with the correct multiplicative biases.

The mock galaxy catalogs represent the intrinsic galaxy distribution at the redshift of galaxy, but do not include the magnification bias effect on the observed galaxy distribution by gravitational lensing by foreground matter fluctuation. We evaluate the contribution of magnification bias to the autocovariance of galaxy-galaxy lensing signals analytically as in Sugiyama *et al.* [70] (see Appendix A of the paper). In this paper, we also evaluate the contribution of magnification bias to cross covariance between galaxy-galaxy lensing and cosmic shear signals. The formulation is summarized in Appendix E.

We note that the redshifts in the mock catalogs were assigned based on the DNNZ estimates due to their availability in time when the covariance calibrations were started. Therefore the mock measurements for the covariance were also performed with a source sample selected based on using the redshift PDFs from DNNZ used in Eq. (1). The covariance in the galaxy-galaxy lensing signal consists of two terms, the shape noise and the covariance due to large-scale structure. The shape noise depends upon the number density of the source galaxy sample, while the large-scale structure term arises independent of the source galaxy sample. The shape noise term dominates on small scales but decreases as we

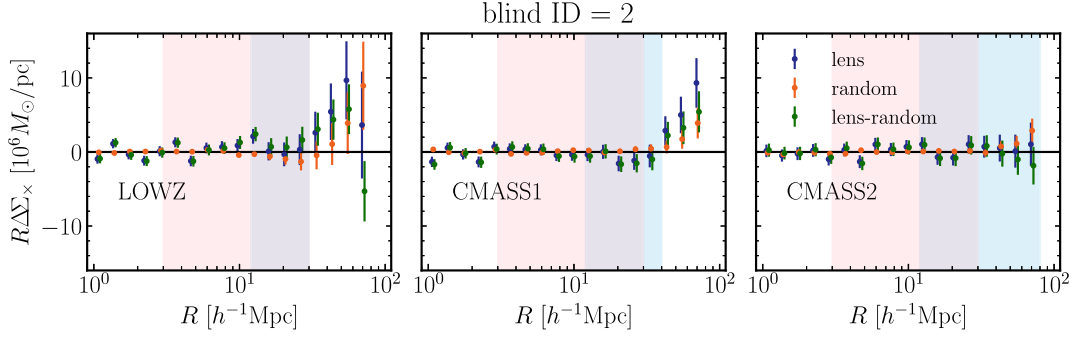


FIG. 10. Systematic test of galaxy-galaxy lensing signal, i.e null test of $\Delta\Sigma_x$. From left to right panels, the cross signal from LOWZ, CMASS1 and CMASS2 subsamples are shown. The blue points shows lensing signal around lens galaxy, the orange points shows signals around random points, and the green points shows the subtracted signal. The sky blue and pink shaded region indicates the scale which the large-scale only analysis and small-scale only analysis uses for cosmology inference.

consider larger and larger separations owing to the larger number of lens-source pairs, where the large scale structure term then can play a dominant part. We measure each of these terms separately [101].

Given that our fiducial sample consists of galaxies selected using redshift PDFs from DEmPz which results in a source sample with a higher source galaxy number density, we scale the shape noise term by the square root of the ratio of the source galaxy number density when selected using DNNZ to that obtained using a selection in DEmPz. We maintain the large-scale structure term as is.

Finally, we also note that the mock galaxy-galaxy lensing signals are used further to estimate the cross covariance with the cosmic shear measurements by combining these measurements with the cosmic shear signals measured from the same set of mock shape catalogs in Sec. VI A.

Figure 7 shows the cumulative signal-to-noise ratio as the function of minimum scale cut. The upper and lower panels are for large- and small-scale analysis, respectively. The total signal-to-noise ratios of our measurements in the LOWZ, CMASS1 and CMASS2 subsamples are 7.6, 11.3, 10.6, respectively for our large-scale analysis. When including the scales that will be modeled in our small-scale analysis, these signal-to-noise ratios increase to 13.4, 17.3, 15.8, respectively.

B. Systematic tests

We carry out a variety of systematic tests in order to validate the measured weak lensing signal. In Fig. 10, we show the cross component of the weak lensing signal for the three subsamples for the fiducial photometric redshift estimates from DNNZ in the three different columns. Figure 21 in Appendix C corresponds to the same measurements but using the photometric redshift codes Mizuki and DEmPz. The blue color points correspond to the measurement around the lens samples, the red ones correspond to the measurement around the random points,

and the green points correspond to the subtraction of the two.

The cross signal is expected to be zero apart from the presence of any systematics. On large scales, we observe a significant deviation from zero in the LOWZ and the CMASS1 subsamples, but we do not see such effect for the CMASS2 subsample. Similarly the lensing signal around random points is also nonzero, but it is not large enough to explain the deviation seen around the lenses. Therefore the cross systematic around the lenses still survives after subtracting the cross signal around random points.

One likely explanation is that the cross systematic appears on a fixed angular scale, and given the redshift differences in each of our subsamples, this angular scale corresponds to a different distance in comoving coordinates for each of our subsamples. The scale where this cross systematic appears is 2.3 deg, which is slightly larger than the HSC field-of-view size, 1.5 deg, beyond which even the random subtraction does not seem to help.

The presence of the cross systematic dictates the large-scale cut we will use for the cosmological analysis of these measurements. We will use large scale cuts of $30h^{-1}$ and $80h^{-1}$ Mpc for the analysis of the signals from the LOWZ, CMASS1, and CMASS2 subsamples, respectively. In our cosmological analyses, we will also adopt cuts on the small scale which are motivated by modeling uncertainties on small scales. The large-scale only analysis which uses perturbation theory based techniques and the small-scale only analysis which uses a halo occupation distribution modeling framework will use small-scale cuts of $12h^{-1}$ Mpc and $3h^{-1}$ Mpc, respectively. In the small-scale analysis, we also discard lensing signals over $R > 30h^{-1}$ Mpc because they give negligible contribution of signal-to-noise ratio compared with smaller scales around $R \sim 3h^{-1}$ Mpc.

We compute the reduced chi-squared $\chi_{\text{red}}^2 = \chi^2/\text{d.o.f.}$ away from a null value of the cross signal around the lens sample after the subtraction of the cross signal around

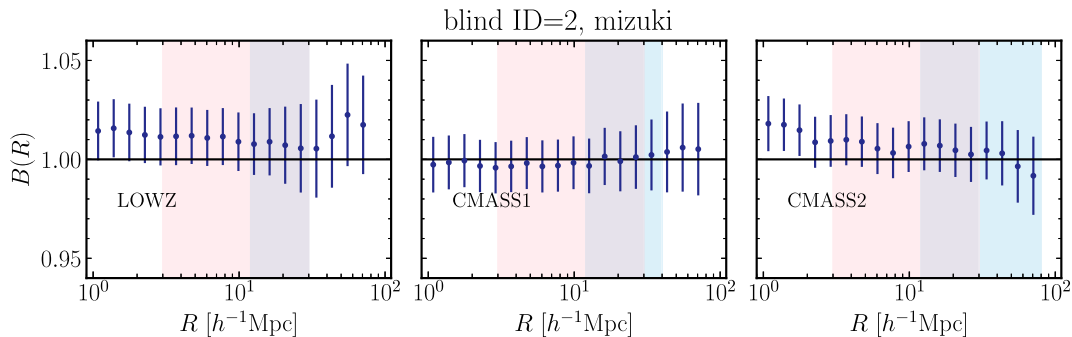


FIG. 11. Systematic test of galaxy-galaxy lensing signal: boost factor for each of the lens subsamples. The boost factor is consistent with unity in the scales of interest for LOWZ, CMASS1 and CMASS2 subsamples with p values greater than 0.10.

random points. These values along with the corresponding p values to exceed the χ^2 given the d.o.f. are also tabulated in Table IV computed over the scales used in the large-scale and small-scale analyses, respectively. These values justify our choice of the scale cuts for our cosmology analysis.

We note that we do see some evidence of cross systematic with p values smaller than 0.05 for the LOWZ and CMASS1 subsamples when using the Mizuki source galaxy sample. This sample of source galaxies has the highest number density, which results in smaller errors. In the bottom panel of Fig. 21, we do not see a systematic deviation in one direction, but the cross points lie above and below the zero line, with a scatter not consistent with the errors on these points. We flag this issue, in case there is an interest in using the Mizuki based source sample for cosmological analyses. We proceed further by noting that our fiducial analysis will rely on the DEmpZ based sample of source galaxies.

Galaxies which are physically correlated with the lens sample could seep into our source samples due to imperfections in the photometric redshift PDFs despite our stringent cuts. Such galaxies are not expected to be efficiently lensed by our sample of lens galaxies. The inclusion of such galaxies could therefore result in a diluted signal. The presence of correlated galaxies in the source sample can be inferred by comparing the number of source galaxies around the lens sample with the number of pairs

around random points. If the source galaxies are correlated, we expect the ratio of the two pair counts, also called the boost factor, to be consistent with unity.

In Fig. 11, we show the boost factor for all three of our lens samples. In the scales of our interest shown as the colored shaded regions, we do not see a significant deviation away from unity. The measurements shown in the figure are expected to be correlated. The chi-squared for the expectation $B(R) = 1$, and the corresponding p values for all three cases for the large-scale and the small-scale analysis are written in Table V. We find that the boost factors are consistent with unity for the LOWZ and CMASS2 samples, although the CMASS1 sample shows p values smaller than 10%. This is related to the large covariance in the measurement of the boost factor and the measurements of boost values which swing from being below unity to above unity in some cases, which results in a large χ^2 . We have verified that if we ignore the covariance then the χ^2 values are small and result in a large p value. Furthermore, the boost factor values in the case of the CMASS1 subsample are away from unity at the subpercent level. Therefore we do not apply any boost factor corrections to our signals.

Just as in the case of the clustering signal we also quantify the variation of the galaxy-galaxy lensing signal with redshift. We measure the galaxy-galaxy lensing signals in subsamples of each redshift bin and present the result in each of the subpanels of Fig. 13. We fit these

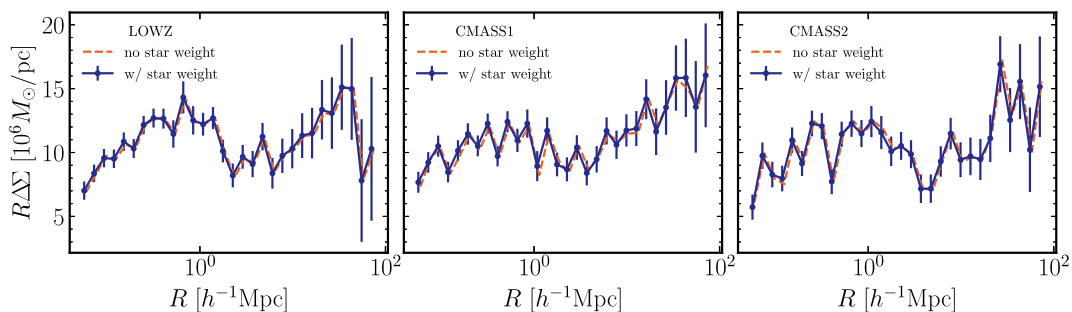


FIG. 12. The variation of the galaxy-galaxy lensing signal with and without systematic weights related to the number density of stars and the seeing. The difference between these signals is within the statistical errors.

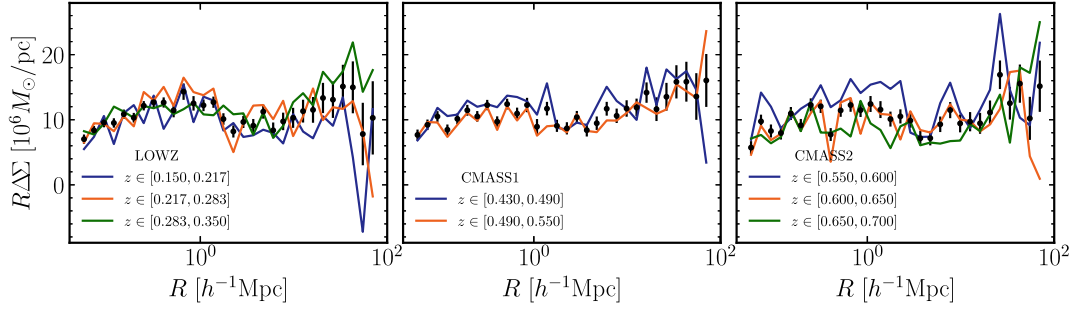


FIG. 13. The variation of the galaxy-galaxy lensing signal in each redshift bin is shown in the three panels. In each panel we show the lensing signal in a given redshift bin by points with errors, while the lensing signal when the redshift bin is further subdivided by solid lines of varying colors. We fit a varying amplitude as a function of redshift in each panel to the solid lines and do not find significant evidence for evolution given the statistical errors.

signals with a fiducial model at the median redshift of the sample with fiducial cosmological parameters with a free amplitude that varies with redshift according to Eq. (33) and again obtain results which indicate a result consistent with no variation at the $2\text{-}\sigma$ level (see Table III). In addition, we also show the very weak dependence of the weak lensing signal whether we use or do not use the systematic weights related to the stellar density in the various sub-panels of Fig. 12.

VI. COSMIC SHEAR MEASUREMENTS

We use the infrastructure described in Sec. III C in order to measure the cosmic shear signal using the common sample of source galaxies used in the galaxy-galaxy lensing measurement. Note that in the 3×2 pt analyses, we do not perform a tomographic measurement of the cosmic shear. In this section, we will present these cosmic shear measurements as well as our estimates of the covariance of these measurements using the mock catalogs. We use a total of 30 logarithmic bins starting from 0.25 arcmin to a maximum distance of 360 arcmin in order to carry out our measurements. As mentioned previously, we will use a single source sample, and not perform any tomographic measurement of the cosmic shear signal. A single source

sample will allow us to self-calibrate any residual source redshift uncertainties.

A. Measurements

We show the measurements of the cosmic shear correlation functions, ξ_+ and ξ_- , in the bottom panels of Fig. 5. Both the measurements approximately scale as $1/\theta$. Although we measure the signals on a wide range of scales, we will only use the signal shown in the shaded regions. The cut on small scales is dictated by our requirement that the modeling uncertainties in the power spectrum due to the impact of baryonic physics do not result in significant biases. To this end, in our companion paper, Miyatake *et al.*, we show that the dark matter only model, compared with various models which account for the uncertain baryonic physics give consistent cosmological inference on scale cuts implemented in this paper. For ξ_+ this corresponds to a small-scale cut of 8 arcmin, while the corresponding cut for ξ_- is equal to 30 arcmin. On large scales, the scale cuts are dictated by systematics in the measured signals as we will describe below.

The measurements of the cosmic shear signals were performed on the mock shape catalogs in order to obtain the covariance of the cosmic shear signals. Note that the mock catalogs themselves were constructed without the inclusion of any multiplicative biases. Therefore, in order to estimate the covariances for the three blind catalogs with nonzero multiplicative biases, we include the multiplicative bias in Eqs. (5) and (6) by changing $\gamma \rightarrow (1 + \hat{m})\gamma$ at the catalog level. The values of the multiplicative bias \hat{m} are taken from the corresponding blind catalog.

As mentioned in the previous section, the mocks were constructed based on the DNNZ photometric redshift estimates. We have measured the mock cosmic shear signals with galaxies from the DNNZ selected source sample. These measurements are then used to measure the covariance matrix. Given the difference in the number density of DNNZ and DEmPz selected source samples, we have rescaled the shot noise related term in the covariance matrix.

TABLE III. The slope of the systematic variation of the lensing signal with redshift for each of the subsamples and the small- and large-scale analyses are presented in the top and bottom sections, respectively. We find no significant evidence of variation with redshift.

Analysis	Sample	α
Small scale	LOWZ	1.6 ± 1.9
	CMASS1	-5.9 ± 3.1
	CMASS2	-4.4 ± 2.2
Large scale	LOWZ	4.3 ± 3.0
	CMASS1	-2.3 ± 4.8
	CMASS2	-2.8 ± 3.3

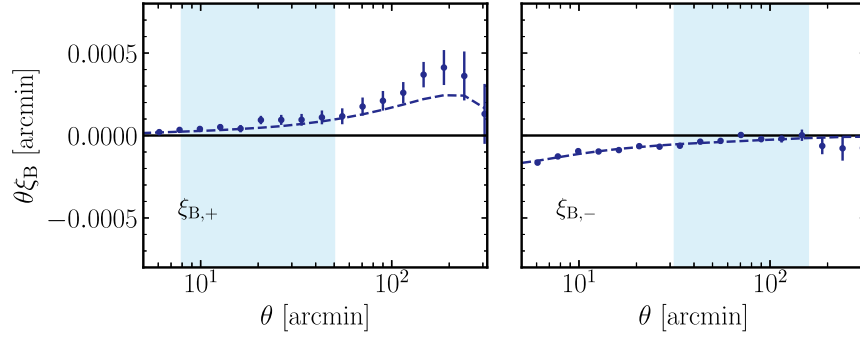


FIG. 14. Systematic test of cosmic shear signal, i.e. B -mode test. The B -mode expectations are consistent with that due to survey geometry effects and are consistent with the expectation from mock catalogs shown as the blue dashed line in each of the panels.

The cross-correlation coefficient of the covariance matrix obtained from our cosmic shear measurements can be seen as two of the blocks in Fig. 6. Since the cosmic shear measurements and the galaxy-galaxy lensing measurements also share the same mock catalogs, we have also obtained the cross covariance between these measurements. Although they are not very large, we do find nonzero cross-correlations between these measurements, which we will take into account in our analyses. The cross-correlation between the clustering and the lensing measurements are considered to be zero, given that the clustering measurements come from the entire SDSS footprint, while the lensing measurements are restricted to HSC regions, which are a small fraction of the entire SDSS footprint.

Figure 7 shows the cumulative signal-to-noise ratio for large- and small-scale analysis as a function of the minimum scale cut. The total signal-to-noise ratios of our measurements for ξ_+ and ξ_- are 20.2 and 19.0, respectively.

B. Systematic tests

In Fig. 14, we present our measurements of the B -mode signals, $\xi_{B,+}$ and $\xi_{B,-}$ computed using the measurements of ξ_+ and ξ_- , respectively, obtained using finer binning to avoid noise. The finite field size of our weak lensing shape catalog regions can result in a residual nonzero B mode in the cosmic shear signals. We evaluate the presence of such residual B -modes using our mock shape catalogs (which do not include any systematics) and present the mean from the mocks as a dashed line. We compute the χ^2 per degree of freedom and the p value for the χ^2 to exceed the one measured in the data (see Table VI). We use the mean mock measurement of the B modes with respect to the measured B modes in our data for the above purpose. We obtain reasonably good χ^2 values with large p values if we restrict ourselves to scales below 50 arcmin for ξ_+ and below 150 arcmin for ξ_- .

We note that this result was obtained after excluding a problematic 20 sq deg area in the GAMA09H region whose inclusion would result in a significantly larger B -mode

signal especially in the cosmic shear tomography analyses presented in Li *et al.* [43] and Dalal *et al.* [44]. We comment on this region in Appendix D.

As discussed in Sec. III C, PSF leakage and residual PSF model error contaminate the measured cosmic shear signal. In our cosmology analyses, we model this contamination as Eq. (29) and add it onto the model prediction of gravitational lensing signal. Here, we present the constraint on coefficients α_{psf} and β_{psf} to be used as prior during cosmological parameter inference. We follow the method in Hamana *et al.* [102]. The coefficients α_{psf} and β_{psf} can be estimated from the cross-correlation functions between $\gamma^{p,q}$ from star catalog and galaxy shears from galaxy shape catalog. These cross-correlation functions can be expressed as

$$\xi_{\pm}^{\text{gp}} = \alpha_{\text{psf}} \xi_{\pm}^{\text{pp}} + \beta_{\text{psf}} \xi_{\pm}^{\text{pq}}, \quad (39)$$

$$\xi_{\pm}^{\text{gq}} = \alpha_{\text{psf}} \xi_{\pm}^{\text{pq}} + \beta_{\text{psf}} \xi_{\pm}^{\text{qq}}. \quad (40)$$

All the correlation functions in the above equations are measurable from star catalogs and galaxy catalogs, and hence α_{psf} and β_{psf} can be estimated. In the following figures, we show the measurement result with stars with flags `i_calib_psf_used=True`. We also perform the same analysis with the stars with flags `i_calib_psf_used=False`, and finally take account of the uncertainty of $\hat{\xi}_{\text{psf},\pm}$ due to the difference of stars whether `i_calib_psf_used=True` or `False`.

Figure 15 shows the cross-correlations between $\gamma^{p,q}$ and galaxy shears. The error bar is estimated from the measurements of mock galaxy shape catalogs and the real star catalog, i.e. the error bar takes account of the cosmic variance. We find that $\xi_{\pm}^{\text{gp},\text{gq}}$ are consistent with zero within the statistical uncertainty, and hence we will focus on the ξ_+ mode alone in the following analysis. Figure 16 shows the autocorrelations of PSF leakage and PSF model error. We first estimate the coefficients α_{PSF} and β_{PSF} as a function of angular separation by fitting signals in each bin in order to check the assumption that coefficients are scale

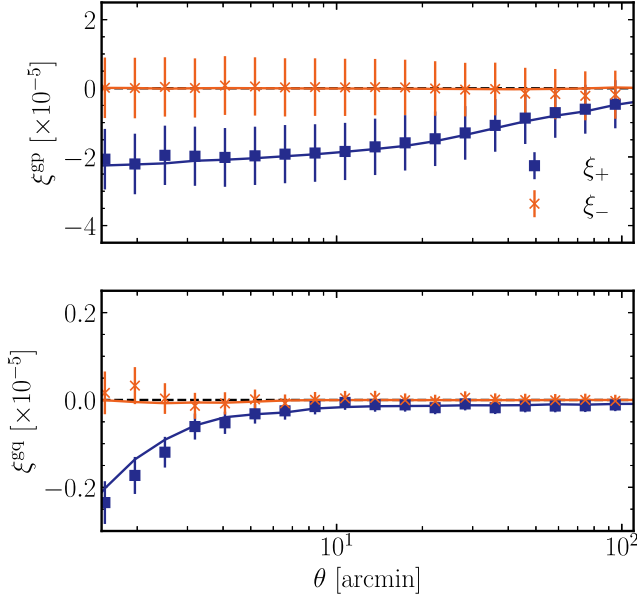


FIG. 15. Cross correlation function between galaxies and PSF ellipticity (γ^p) and the PSF model error (γ^q) are shown in the upper and lower panels, respectively. We model these functions to determine the values of the PSF systematics model parameters, α_{psf} and β_{psf} .

independent. The result is shown in Fig. 17, indicating that the coefficients are scale invariant within the statistical uncertainty. Combining the coefficient estimates over the scales for cosmology analyses indicated by the blue shaded region, we estimate the mean coefficients and the errors on them, shown in the horizontal orange line and shaded region.

The orange contour in Fig. 18 shows the constraint on the coefficients using stars with flags `i_calib_psf_used=True`, while the green contour shows with flags `i_calib_psf_used=False`. These contours are two-dimensional Gaussian distribution, because Eqs. (39)

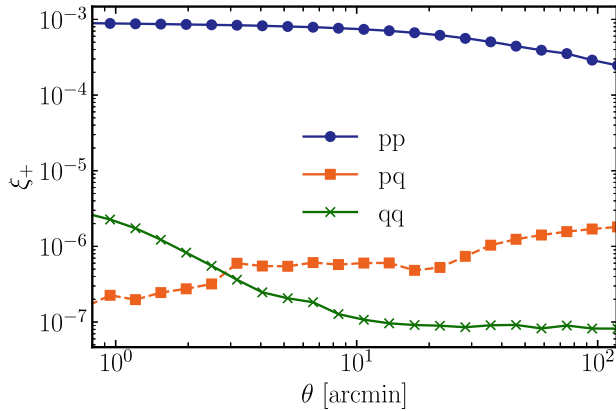


FIG. 16. Autocorrelation and cross-correlation functions of the PSF ellipticity (γ^p) and the PSF model error (γ^q). The contribution of each of these to the cosmic shear correlation functions are governed by the parameters α_{psf} and β_{psf} .

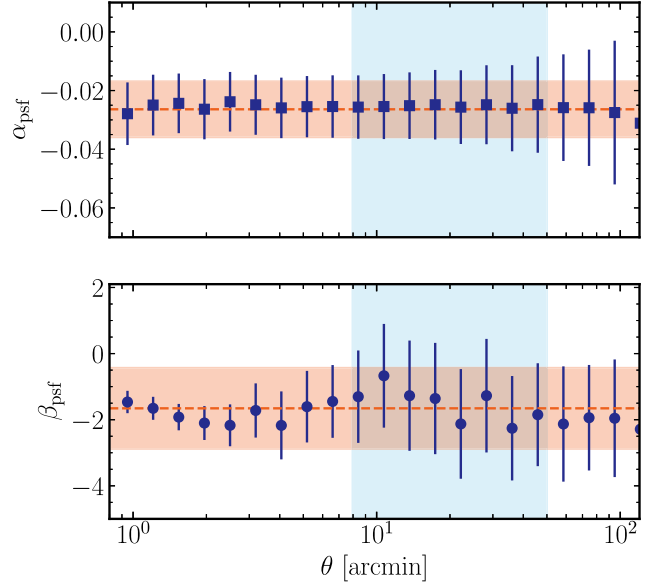


FIG. 17. The scale dependence of the PSF systematic coefficients α_{psf} and β_{psf} , obtained by fitting the correlation functions shown in Fig. 15. We do not observe any significant scale dependence in the values of these PSF systematics coefficients.

and (40) are linear in α_{psf} and β_{psf} . The coefficients from the orange and green contour predict slightly different ξ_{\pm}^{psf} . We find that this uncertainty of ξ_{\pm}^{psf} due to the difference of stars whether `i_calib_psf_used=True` or `False` can be covered by rescaling the statistical uncertainty of orange

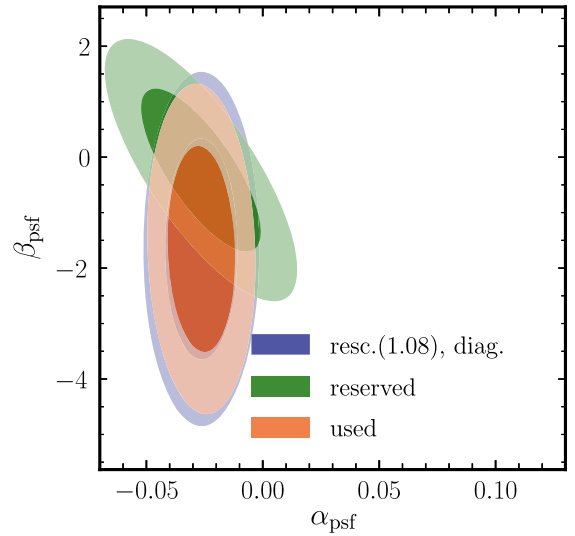


FIG. 18. Constraint on α_{psf} and β_{psf} parameters. The orange and green contours show the constraints on $(\alpha_{\text{psf}}, \beta_{\text{psf}})$ using stars selected by `i_calib_psf_used=True` and `False`, respectively. The blue contour is the diagonalized Gaussian posterior with respect to α and β , and the posterior size is rescaled by a factor of 1.08 to cover the uncertainty $\xi_{\text{psf},+}$ due to the choice of star selection, i.e. `i_calib_psf_used=True` or `False`. The blue contour is used as a conservative prior on α_{psf} and β_{psf} in the cosmology analyses.

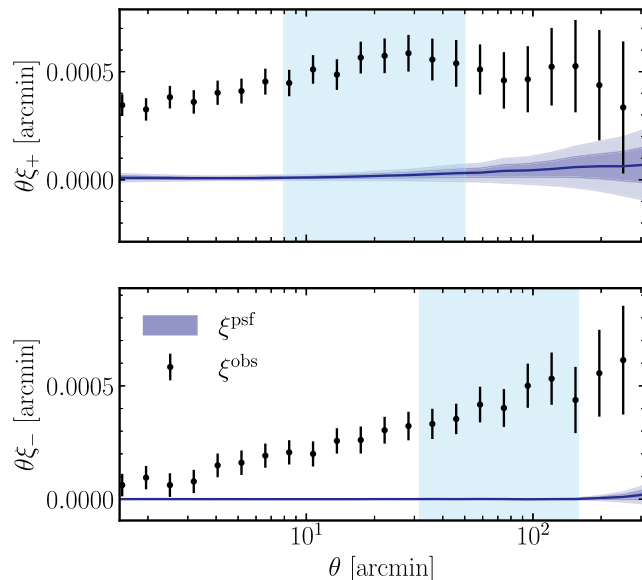


FIG. 19. Posterior distribution of PSF correlation term which contaminates the observed cosmic shear correlation function. The measured cosmic shear correlation functions are much larger than the contamination from PSF systematics.

contour by a factor of 1.08 [103]. For simplicity, we also diagonalize the rescaled constraint with respect to α_{psf} and β_{psf} , which will be used in the cosmology analyses. In Fig. 19, we compare the posterior distribution of the PSF correlation term with the cosmic shear correlations and observe that the contamination from PSF systematics is much smaller than the measured signals.

VII. SUMMARY

A joint analysis of the three two-point functions: the galaxy clustering signal, the galaxy-galaxy lensing signal and the cosmic shear signal is a unique probe of cosmology. In a series of papers, based on imaging data obtained over a three year period from the HSC survey and the spectroscopic data from the SDSS, we will present the cosmological constraints on the matter density parameter as well as the amplitude of density fluctuations. In this paper, the first in the series, we present robust measurements and systematic tests corresponding to the measurement of each of the above signals. Please note that bullets are not used in PRD papers. Adjustments have been made accordingly. A summary of the results and products made available in this paper are as follows:

(1) We define three different subsamples of spectroscopic lens galaxies from the large-scale structure samples of SDSS-BOSS galaxies. These subsamples are defined to be approximately volume limited by absolute magnitude ($k+e$ corrected), the LOWZ, CMASS1 and CMASS2 subsamples of galaxies with $z \in [0.15, 0.35]$, $[0.43, 0.55]$ and $[0.55, 0.70]$, respectively, and absolute magnitude of galaxies of $M_i - 5 \log h < -21.5$, -21.9 , and -22.2 for the three subsamples, respectively.

(2) We conservatively define a single subsample of source galaxies from the HSC-Y3 shape catalog that we use for the weak lensing signals to be measured in this paper. Our subsample of galaxies has a greater than 99% probability assigned by the photometric redshift assignment algorithm DEmPz to be above a redshift of 0.75, higher than the redshift of any of our lens subsamples by more than $dz = 0.05$. We also present the inferred redshift distribution of our source galaxies based on the method presented in [62].

(3) We have generated 108 mock catalogs for our subsample of SDSS galaxies to aid in the computation of the covariance matrix of their clustering signal. These mock catalogs were created by populating halos with galaxies with a halo occupation distribution designed to reproduce the abundance and clustering of the galaxy subsamples we use on scales of $0.5h^{-1} \text{ Mpc} > R > 80h^{-1} \text{ Mpc}$. Our mock catalogs further mimic the footprint of the SDSS survey.

(4) We have also generated 1404 mock shape catalogs of galaxies by randomly rotating the ellipticities of galaxies in our HSC-Y3 shape catalog, and distorting them with shears that would arise from the large-scale structure distribution in a Λ CDM universe. These mock catalogs aid in the computation of the covariance of the two point measurements involving weak gravitational lensing shears.

(5) We describe the codes and pipelines used to optimally perform the three two-point correlation function measurements on data as well as on the mock catalogs in order to estimate the full covariance matrix of our observables.

(6) Based on the clustering pipeline, we present the measurements of the projected clustering signal of the three subsamples of galaxies. In the range of scale cuts over which we will perform our cosmological analyses with the large-scale perturbation theory-based model (Paper III), the signal-to-noise ratio of the clustering signals are 25.6, 27.6, 26.6 for the LOWZ, CMASS1 and CMASS2 subsamples, respectively. When including the small scales that will be modeled in Paper II, the corresponding signal-to-noise ratios are 38.5, 37.1, 35.7, respectively.

(7) We also show that the clustering signals within each subsample do not change substantially irrespective of the use of systematic weights, suggested by the SDSS-BOSS team, that are related to the number density of stars or seeing in the SDSS imaging data used to define the spectroscopic targets. We also show that the clustering signal of our subsample of galaxies does not show substantial evidence for variation within different redshift bins.

(8) Using the weak lensing pipeline, we present our measurements of the galaxy-galaxy lensing signal for each of our lens subsamples using the single source galaxy sample. For the large-scale analyses, the signal-to-noise ratio of the galaxy-galaxy lensing signals is 7.6, 11.3 and 10.6, for the LOWZ, CMASS1, and CMASS2 subsamples, respectively. The corresponding signal-to-noise ratios for the measurements in the scales of interest relevant to small-scale analysis are 13.4, 17.3 and 15.8, respectively.

(9) We presented a number of systematic tests for the weak lensing signals: the null signals around random points, the null cross signals, corresponding to each of our subsamples of galaxies. We also presented that the contamination of our measured signals due to the presence of source galaxies physically associated with our lens galaxies is negligible due to our conservative source selection. We have further shown that the measured lensing signals are not impacted by the use of the systematic weights corresponding to the SDSS-BOSS large-scale structure subsamples. The lensing signal amplitudes within the redshift bin for each subsample also show no significant variation as a function of redshift.

(10) We also presented the measurements of the cosmic shear correlation functions ξ_{\pm} for our source galaxy sample. The signal-to-noise ratio of our measurements of ξ_{+} and ξ_{-} are 20.2 and 19.0, respectively. We also presented systematic tests for the cosmic shear measurements including a decomposition into E and B modes. The largest scales of interest for the cosmological analyses were chosen based on the null detection of B modes, while the smallest scales were chosen based on the accuracy of our theoretical templates.

(11) Finally, we also presented our best estimates for the PSF systematic parameters α_{PSF} and β_{PSF} which quantify the PSF leakage and the residual PSF model error. The values we obtain will be used in the cosmological analyses to model the PSF systematic component of the cosmic shear signal, in order to marginalize over these nuisance parameters.

The measurements presented in this paper, the covariances and the constraints on parameter systematics have been used in the 3×2 pt analysis of the data to infer the constraints on the cosmological parameters Ω_m and σ_8 , in particular the parameter combination, S_8 . These results will be presented in our companion papers Sugiyama *et al.* [42] and Miyatake *et al.* [41].

The Subaru Hyper Suprime Cam survey has also finished collecting data from its entirety of operations which spanned 330 nights in total. The wide survey area which is the most useful in terms of its cosmological constraining power will span a total of about 1100 sq deg. Numerous challenges will be involved in the processing of data with such statistical power, in particular, to keep the systematic error budget under control. As we will show in the companion papers, the photometric redshift uncertainties are still our dominant source of errors. Addressing this challenge using additional measurements, better data as well as innovative techniques are going to be a necessary task before the arrival of data from the Rubin LSST.

ACKNOWLEDGMENTS

We thank the anonymous referee for a careful reading of the manuscript and the constructive inputs on the version of the manuscript submitted for review. This work was supported in part by World Premier International Research

Center Initiative (WPI Initiative), MEXT, Japan, and JSPS KAKENHI Grants No. JP18H04350, No. JP18H04358, No. JP19H00677, No. JP19K14767, No. JP20H00181, No. JP20H01932, No. JP20H04723, No. JP20H05850, No. JP20H05855, No. JP20H05856, No. JP20H05861, No. JP21J00011, No. JP21H05456, No. JP21J10314, No. JP21H01081, No. JP21H05456, No. JP22H00130, No. JP22K03634, No. JP22K03655, No. JP22K21349, No. JP23H00108 and No. JP23H04005; by JSPS Core-to-Core Program (Grant No. JPJSCCA20210003); by Japan Science and Technology Agency (JST) CREST JPMHCR1414; by JST AIP Acceleration Research Grant No. JP20317829, Japan; and by Basic Research Grant (Super AI) of Institute for AI and Beyond of the University of Tokyo. S. S. was supported in part by International Graduate Program for Excellence in Earth-Space Science (IGPEES), WINGS Program, the University of Tokyo. R. D. acknowledges support from the NSF Graduate Research Fellowship Program under Grant No. DGE-2039656. Y. K. is supported in part by the David and Lucile Packard foundation. W. L. acknowledges the support from the National Key R&D Program of China (2021YFC2203100), the 111 Project for ‘‘Observational and Theoretical Research on Dark Matter and Dark Energy’’ (B23042), NSFC (No. 11833005, No. 12192224) as well as the Fundamental Research Funds for the Central Universities (WK3440000006). The Hyper Suprime-Cam (HSC) Collaboration includes the astronomical communities of Japan and Taiwan, and Princeton University. The HSC instrumentation and software were developed by the National Astronomical Observatory of Japan (NAOJ), the Kavli Institute for the Physics and Mathematics of the Universe (Kavli IPMU), the University of Tokyo, the High Energy Accelerator Research Organization (KEK), the Academia Sinica Institute for Astronomy and Astrophysics in Taiwan (ASIAA), and Princeton University. Funding was contributed by the FIRST program from the Japanese Cabinet Office, the Ministry of Education, Culture, Sports, Science and Technology (MEXT), the Japan Society for the Promotion of Science (JSPS), Japan Science and Technology Agency (JST), the Toray Science Foundation, NAOJ, Kavli IPMU, KEK, ASIAA, and Princeton University. This paper makes use of software developed for the Large Synoptic Survey Telescope. We thank the LSST Project for making their code available as free software at [104]. The Pan-STARRS1 Surveys (PS1) have been made possible through contributions of the Institute for Astronomy, the University of Hawaii, the Pan-STARRS Project Office, the Max-Planck Society and its participating institutes, the Max Planck Institute for Astronomy, Heidelberg and the Max Planck Institute for Extraterrestrial Physics, Garching, Johns Hopkins University, Durham University, the University of Edinburgh, Queen’s University Belfast, the Harvard-Smithsonian Center for Astrophysics, the Las

Cumbres Observatory Global Telescope Network Incorporated, the National Central University of Taiwan, the Space Telescope Science Institute, the National Aeronautics and Space Administration under Grant No. NNX08AR22G issued through the Planetary Science Division of the NASA Science Mission Directorate, the National Science Foundation under Grant No. AST-1238877, the University of Maryland, and Eotvos Lorand University (ELTE) and the Los Alamos National Laboratory. The measurements presented in this manuscript are based in part on data collected at the Subaru Telescope and retrieved from the HSC data archive system, which is operated by Subaru Telescope and Astronomy Data Center at National Astronomical Observatory of Japan.

APPENDIX A: SYSTEMATIC DIFFERENCES IN THE INFERRED REDSHIFT DISTRIBUTION

As shown in Fig. 2, we see differences in the inferred redshift distribution of our source sample depending upon whether we use the redshift PDFs from D_{EmPz} or D_{NNZ} . We estimate the potential biases in the measured weak lensing signals due to these systematic uncertainties.

For the galaxy-galaxy lensing signal this systematic bias can be quantified by computing the average ratio of the critical surface density of the source sample (described in Sec. II A) by utilizing the inferred redshifts from either of the two estimates. We compute this ratio by using the median redshifts of each of our lens samples (described in Sec. II C). We find that for the LOWZ sample the critical surface density based on the redshifts inferred based on D_{EmPz} is higher by 1.7% compared with those inferred based on D_{NNZ} , while this difference grows to 3.3% and 4.2% for the CMASS1 and CMASS2 subsamples.

For the cosmic shear signal, we compute the theoretical estimate of ξ_+ and ξ_- for the source sample for the Planck cosmological model using either of the two inferred redshift distributions. For the cosmic shear signal, we also find that the signals based on the redshifts inferred from D_{EmPz} are predicted to be about 6% higher than that from D_{NNZ} .

We would like to have a simple way to parametrize these differences and marginalize over them in our cosmology analysis. We find that the average redshift of the source sample based on the inferred redshift distribution from D_{EmPz} is higher than that of D_{NNZ} by $\Delta\bar{z}$ of 0.04. If we simply shift the inferred redshift distribution from D_{EmPz} lower by the same amount while maintaining the shape of the redshift distribution, we can account for almost all of the differences. When such a shift is included, the ratios of the values of the critical surface density for each of the lens subsamples is reduced to subpercent levels ($<0.75\%$), while the cosmic shear signals also agree at the subpercent level. We recommend the use of such Δz in the systematic uncertainty analyses for cosmological inference. This is particularly important because we do not have any clustering measurements which can constrain the redshift PDFs at high redshifts for our source galaxy sample.

As will be shown in our companion paper Miyatake *et al.* [41], using the self calibration technique of Oguri and Takada [60], there are hints that support a value of Δz of the order -0.06 (albeit at low significance), indicating that the true mean redshifts may possibly be even higher than that suggested by D_{EmPz} .

APPENDIX B: THE VARIATION OF THE SIGNAL IN THE REDSHIFT BIN WITH BOSS FULL SAMPLE

In this section, we present the variation of the clustering signal with the BOSS full sample, i.e the flux limited sample. We used all the galaxies in the SDSS DR11 BOSS catalogs, rather than applying the luminosity cuts used in the main part of this paper. Using this BOSS full sample, we tested the variation of the clustering signal in each redshift in a similar way as Sec. IV B: we divide the galaxies into three or two subsamples in each redshift bin and measure the clustering signal in each subsample. Figure 20 shows the variation of the clustering signal in each redshift bin using the BOSS full sample. Comparing to Fig. 9, we can find that the flux limited sample shows the stronger variation, indicating a stronger evolution of the

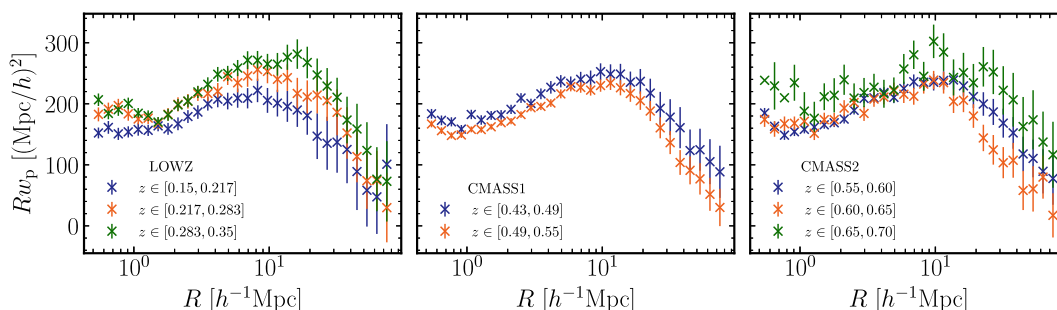


FIG. 20. Similar plot as Fig. 9, but we use the BOSS full sample for the clustering measurements rather than the luminosity limited sample, which is the fiducial lens sample used in this paper.

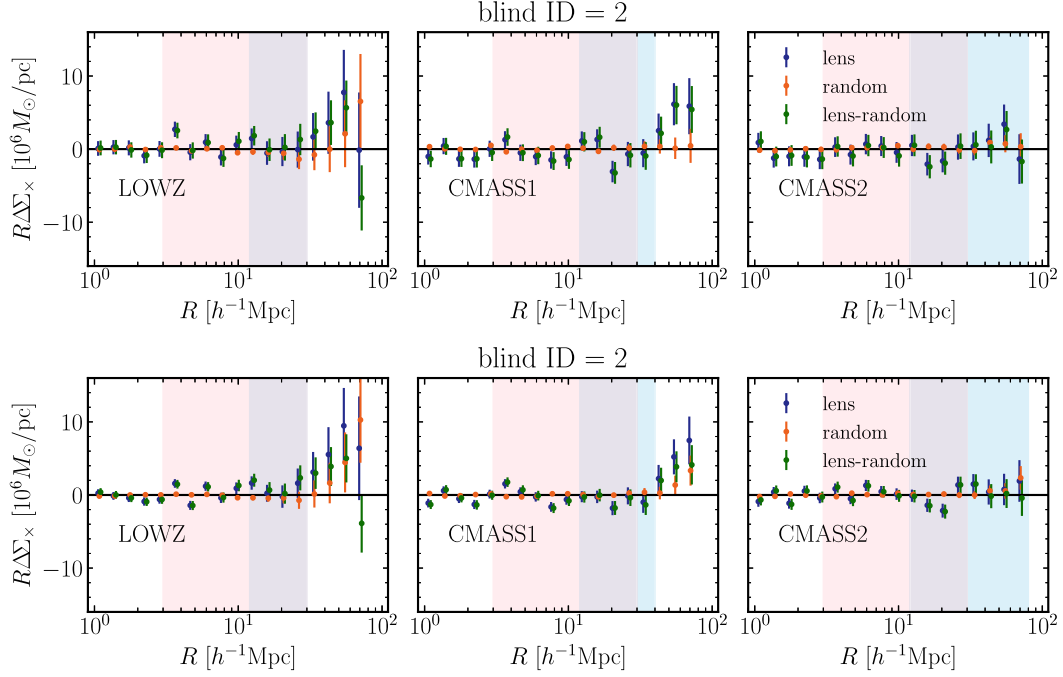


FIG. 21. Similar plot as Fig. 10, but using DNNZ and Mizuki for sample selection.

galaxy property as a function of redshift. Therefore, the luminosity-limited sample has almost the same galaxy property, and we can model the galaxy physics with a single set of the galaxy-related parameters, e.g. the HOD parameters or galaxy bias parameter, without accounting for the redshift evolution of the galaxy-related parameters in the model in each redshift bin.

APPENDIX C: MEASUREMENTS WITH DNNZ AND Mizuki

In this Appendix, we present the weak lensing measurements and the systematic tests but for the source samples selected using DNNZ and Mizuki, respectively. The upper and lower panels of Fig. 21 present the cross signal measured for the three subsamples of lenses we use for our measurements for the two different source samples. The same comments apply as were observed for the DEmPz based source sample, as written in Sec. VA. We apply the same scale cuts and show the χ^2 and the corresponding p values in Table IV for the large- and small-scale analyses, respectively.

We also compute the boost factors for the corresponding lens subsamples to estimate the contamination of the signal due to galaxies physically associated with the lens sample. These are shown in Fig. 22. The deviation of these signals from unity and the values of the corresponding χ^2 per degree of freedom and the p values, on scales that we will use for our cosmological analyses are listed in Table V.

The B modes from the cosmic shear measurements for the source subsamples selected by the two methods are shown in Fig. 23. In the scales that we consider for our analyses, the B-mode signals are consistent with zero, as in the fiducial analysis (see Table VI).

The galaxy-galaxy lensing measurements, the cosmic shear measurements as well as the redshift distributions for the source samples will be presented in electronic form on the data repository.

TABLE IV. Summary of systematics test of galaxy-galaxy lensing: lensing cross mode. The chi-square, degree of freedom (d.o.f.) and p value are shown in the format of $\chi^2/\text{d.o.f.}(p)$. Different columns show the results for large-scale analysis and small-scale analysis, where χ^2 is computed over the scale of cosmology analyses indicated by blue and red shaded regions in Fig. 10.

Photo-z	Lens sample	Large scale	Small scale
DEmPz	LOWZ	7.57/4 (0.11)	16.65/9 (0.05)
	CMASS1	4.87/5 (0.43)	6.86/9 (0.65)
	CMASS2	3.84/8 (0.87)	7.78/9 (0.56)
DNNZ	LOWZ	2.28/4 (0.68)	10.47/9 (0.31)
	CMASS1	7.14/5 (0.21)	12.56/9 (0.18)
	CMASS2	5.48/8 (0.71)	4.98/9 (0.84)
Mizuki	LOWZ	7.47/4 (0.11)	25.05/9 (0.003)
	CMASS1	4.69/5 (0.45)	20.47/9 (0.02)
	CMASS2	11.03/8 (0.20)	15.56/9 (0.08)

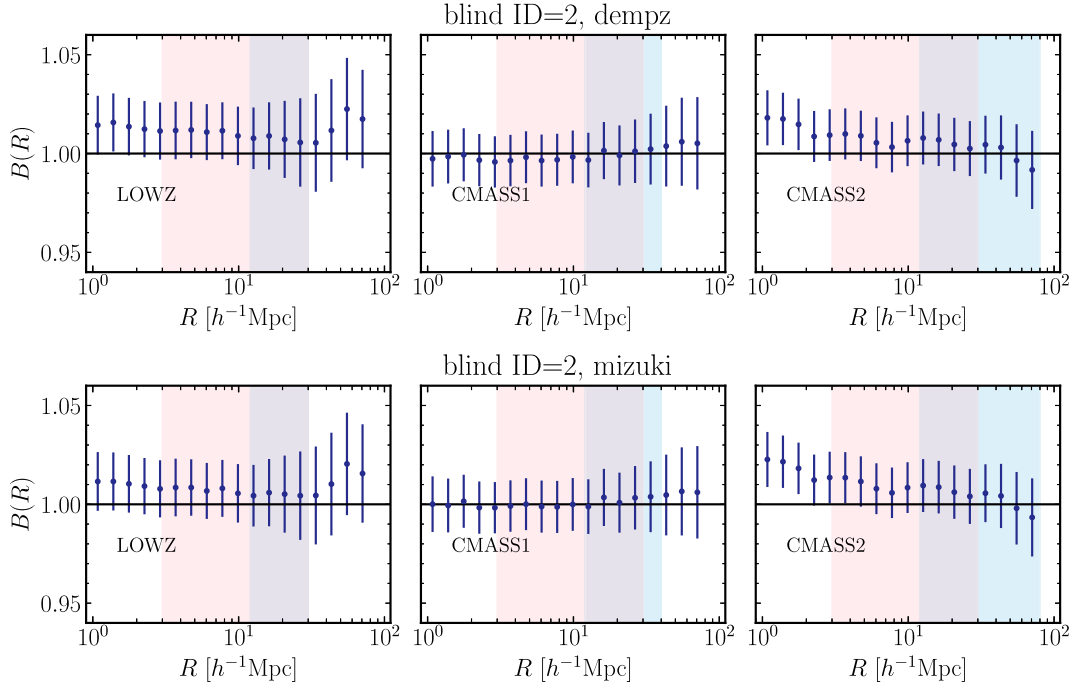


FIG. 22. Similar plot as Fig. 11, but using DNNZ and Mizuki for sample selection.

TABLE V. Summary of systematics of galaxy-galaxy lensing: boost factor. The format is similar to Table IV.

Photo-z	Lens sample	Large scale	Small scale
DEmPz	LOWZ	0.89/4 (0.93)	2.85/9 (0.97)
	CMASS1	10.80/5 (0.06)	15.41/9 (0.08)
	CMASS2	6.61/8 (0.58)	8.16/9 (0.52)
DNNZ	LOWZ	0.76/4 (0.94)	3.28/9 (0.95)
	CMASS1	12.22/5 (0.03)	14.83/9 (0.10)
	CMASS2	8.49/8 (0.39)	8.77/9 (0.46)
Mizuki	LOWZ	0.52/4 (0.97)	3.26/9 (0.95)
	CMASS1	11.21/5 (0.05)	13.83/9 (0.13)
	CMASS2	6.22/8 (0.62)	8.06/9 (0.53)

 TABLE VI. Summary of cosmic shear B -mode null tests. χ^2 is defined as the deviation from mean signal of mock measurements indicated by the dotted line in Figs. 14 and 23.

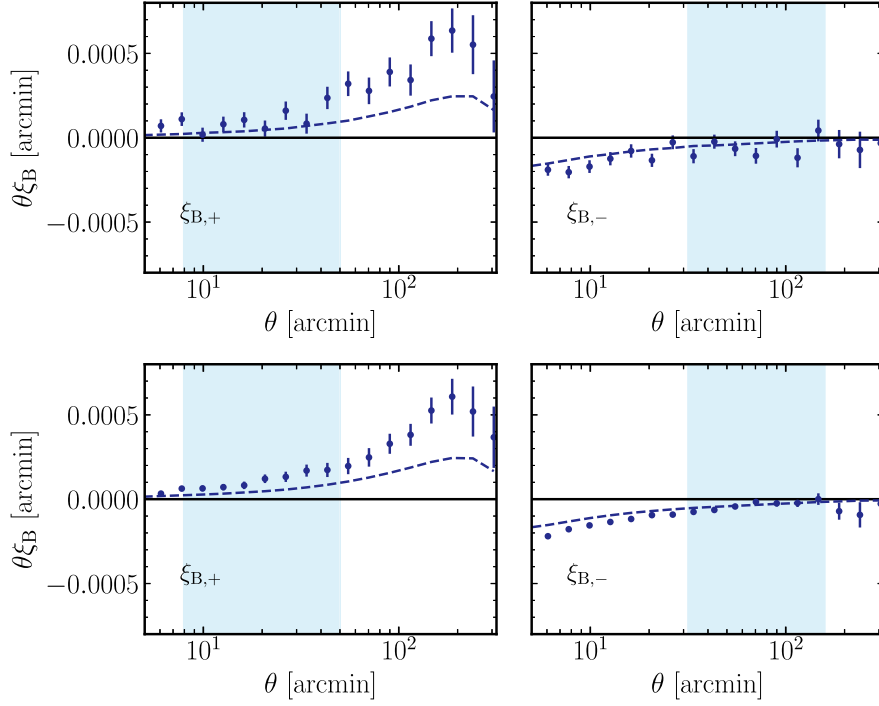
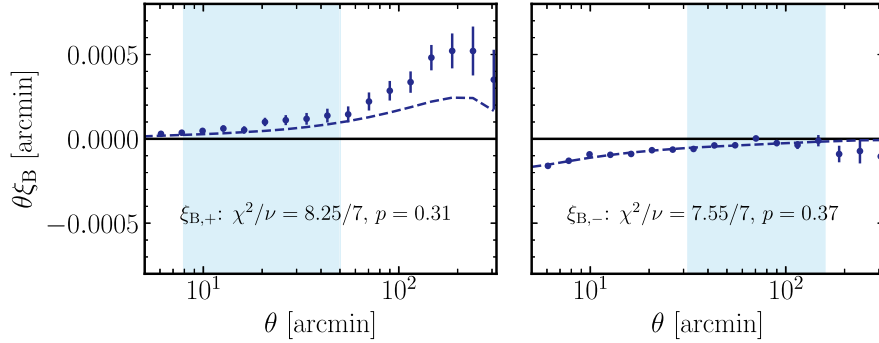
Photo-z	Signal	χ^2/ν (p)
DEmPz	$\xi_{B,+}$	8.81/7 (0.27)
	$\xi_{B,-}$	6.87/7 (0.44)
DNNZ	$\xi_{B,+}$	11.20/7 (0.13)
	$\xi_{B,-}$	9.94/7 (0.19)
Mizuki	$\xi_{B,+}$	11.44/7 (0.12)
	$\xi_{B,-}$	6.89/7 (0.44)

APPENDIX D: A PROBLEMATIC REGION IN GAMA09H FIELD

We have computed the cosmic shear signal using source galaxies selected from DEmPz from the entire full depth full color region of the HSC-Y3 shape catalog. In Fig. 24, we present the B-mode signals measured based on ξ_+ and ξ_- and compare them to the mean expectation from mock shape catalogs. The p value for the B modes computed from ξ_+ show somewhat low values of 0.07, although it is not troublingly low. However, when we had performed this analysis previously with a sample based on DNNZ selection, we had noticed unacceptably low p values, driven partly by the larger amplitude of the B-mode signal from ξ_+ , and the erratic behavior of the B mode signal from ξ_- . By performing a field-by-field analysis with the DNNZ sample, we were able to track down such odd behavior to one of the subfields within HSC, namely GAMA09H. We were able to identify a 20 sq degree region bounded by right ascension between 132.5 and 140.0 deg and declination between 1.6 and 4.7 deg. We have not been able to entirely track down the cause of this issue yet, but empirically this excluded region includes an area which was observed in some of the best seeing conditions. Therefore, to be on the safe side, we carry out all our measurements of the galaxy-galaxy lensing signal and the cosmic shear signal by excluding that particular patch of the sky.

APPENDIX E: ANALYTIC EXPRESSION OF MAGNIFICATION BIAS COVARIANCE

In this section, we derive the analytic expression of magnification bias effect on the cross covariance between

FIG. 23. Systematic test of cosmic shear signal, i.e. B -mode test for the DNNZ and the Mizuki for sample selections.FIG. 24. Cosmic shear B mode test with the problematic region in GAMA09H field.

galaxy-galaxy lensing signal and cosmic shear signal. We consider the galaxy-galaxy lensing of the lens at the representative redshift z_1 and the source sample at source

bin z , and the cosmic shear signal of the source samples at source bin z_{s_1} and z_{s_2} . Considering only the Gaussian terms, the cross covariance is expressed as

$$\begin{aligned}
 & \text{Cov}[\hat{\Delta}\Sigma(R_n, z_l, z_{s_0}), \hat{\xi}_{\pm}(\theta_m, z_{s_1}, z_{s_2})] \\
 &= \Sigma_{\text{cr}}(z_1, z_{s_0}) \frac{1}{\Omega_s} \int \frac{\ell d\ell}{2\pi} J_2\left(\ell \frac{R_n}{\chi_l}\right) J_{0/4}(\ell\theta_m) \left[C_{g\kappa_s}(\ell; z_1, z_{s_1}) \left(C_{\kappa_s\kappa_s}(\ell; z_{s_0}, z_{s_2}) + \frac{\sigma_e^2}{\bar{n}_{s_0}} \delta_{s_0, s_2}^{\text{K}} \right) \right. \\
 &+ C_{g\kappa_s}(\ell; z_1, z_{s_2}) \left(C_{\kappa_s\kappa_s}(\ell; z_{s_0}, z_{s_1}) + \frac{\sigma_e^2}{\bar{n}_{s_0}} \delta_{s_0, s_1}^{\text{K}} \right) + 2(\alpha_{\text{mag}, l} - 1) \left(C_{\kappa_1\kappa_s}(\ell; z_1, z_{s_1}) \left(C_{\kappa_s\kappa_s}(\ell; z_{s_0}, z_{s_2}) + \frac{\sigma_e^2}{\bar{n}_{s_0}} \delta_{s_0, s_2}^{\text{K}} \right) \right. \\
 &\left. \left. + C_{\kappa_1\kappa_s}(\ell; z_1, z_{s_2}) \left(C_{\kappa_s\kappa_s}(\ell; z_{s_0}, z_{s_1}) + \frac{\sigma_e^2}{\bar{n}_{s_0}} \delta_{s_0, s_1}^{\text{K}} \right) \right) \right]. \tag{E1}
 \end{aligned}$$

Here the angular correlation functions C_{XY} are defined in Appendix A of Sugiyama *et al.* [70]. σ_e^2/\bar{n}_{s_0} is the shape noise term of the source sample in redshift bin z , and $\delta_{X,Y}^K$ is the Kronecker delta. R_n and θ_m are the m -th and n -th angular bin of galaxy-galaxy lensing and cosmic shear respectively. J_n is the n -th order Bessel function, and J_0 and J_4 are for ξ_+ and ξ_- respectively. $\alpha_{\text{mag},l}$ is the magnification bias parameter of lens sample z_l . The last two terms are the contribution of the magnification bias effect. In this paper, we have a single source sample, i.e. $z_{s_0} = z_{s_1} = z_{s_2} \equiv z_s$, and hence the

contribution from magnification bias effect to be added on the covariance estimated from mock measurements in Secs. VA and VIA is

$$\begin{aligned} & \delta\text{Cov}[\Delta\Sigma(R_n, z_l, z_s), \xi_{\pm}(\theta_m, z_s, z_s)] \\ &= 2\Sigma_{\text{cr}}(z_l, z_s) \frac{1}{\Omega_s} \int \frac{\ell d\ell}{2\pi} J_2\left(\ell \frac{R_n}{\chi_l}\right) J_{0/4}(\ell\theta_m) 2(\alpha_l - 1) \\ & \quad \times C_{\kappa_1\kappa_s}(\ell; z_l, z_s) \left(C_{\kappa_s\kappa_s}(\ell; z_s, z_s) + \frac{\sigma_e^2}{\bar{n}_s} \right). \end{aligned} \quad (\text{E2})$$

-
- [1] P. A. R. Ade, N. Aghanim, M. Arnaud, M. Ashdown, J. Aumont, C. Baccigalupi, A. J. Banday, R. B. Barreiro, J. G. Bartlett *et al.* (Planck Collaboration), *Astron. Astrophys.* **594**, A13 (2016).
- [2] N. Aghanim, Y. Akrami, M. Ashdown, J. Aumont, C. Baccigalupi, M. Ballardini, A. J. Banday, R. B. Barreiro, N. Bartolo, S. Basak, R. Battye, K. Benabed, J. P. Bernard, M. Bersanelli, P. Bielewicz, J. J. Bock, J. R. Bond, J. Borrill, F. R. Bouchet, F. Boulanger *et al.* (Planck Collaboration), *Astron. Astrophys.* **641**, A6 (2020).
- [3] D. M. Scolnic, D. O. Jones, A. Rest, Y. C. Pan, R. Chornock, R. J. Foley, M. E. Huber, R. Kessler, G. Narayan, A. G. Riess, S. Rodney, E. Berger, D. J. Brout, P. J. Challis, M. Drout *et al.*, *Astrophys. J.* **859**, 101 (2018).
- [4] A. J. Ross, F. Beutler, C.-H. Chuang, M. Pellejero-Ibanez, H.-J. Seo, M. Vargas-Magaña, A. J. Cuesta, W. J. Percival, A. Burden, A. G. Sánchez, J. N. Grieb, B. Reid, J. R. Brownstein, K. S. Dawson, D. J. Eisenstein *et al.*, *Mon. Not. R. Astron. Soc.* **464**, 1168 (2017).
- [5] F. Beutler, H.-J. Seo, A. J. Ross, P. McDonald, S. Saito, A. S. Bolton, J. R. Brownstein, C.-H. Chuang, A. J. Cuesta, D. J. Eisenstein, A. Font-Ribera, J. N. Grieb, N. Hand, F.-S. Kitaura, C. Modi *et al.*, *Mon. Not. R. Astron. Soc.* **464**, 3409 (2017).
- [6] S. Alam, M. Aubert, S. Avila, C. Balland, J. E. Bautista, M. A. Bershad, D. Bizyaev, M. R. Blanton, A. S. Bolton, J. Bovy, J. Brinkmann, J. R. Brownstein, E. Burtin, S. Chabanier, M. J. Chapman *et al.*, *Phys. Rev. D* **103**, 083533 (2021).
- [7] S. Aiola, E. Calabrese, L. Maurin, S. Naess, B. L. Schmitt, M. H. Abitbol, G. E. Addison, P. A. R. Ade, D. Alonso, M. Amiri, S. Amodeo, E. Angile, J. E. Austermann, T. Baillon, N. Battaglia *et al.*, *J. Cosmol. Astropart. Phys.* **12** (2020) 047.
- [8] P. S. Chabul, C. L. Reichardt, N. Gupta, B. Ansarinejad, K. Aylor, L. Balkenhol, E. J. Baxter, F. Bianchini, B. A. Benson, L. E. Bleem, S. Bocquet, J. E. Carlstrom, C. L. Chang, T. M. Crawford, A. T. Crites *et al.*, *Astrophys. J.* **931**, 139 (2022).
- [9] A. G. Sánchez, R. Scoccimarro, M. Crocce, J. N. Grieb, S. Salazar-Albornoz, C. Dalla Vecchia, M. Lippich, F. Beutler, J. R. Brownstein, C.-H. Chuang, D. J. Eisenstein, F.-S. Kitaura, M. D. Olmstead, W. J. Percival, F. Prada *et al.*, *Mon. Not. R. Astron. Soc.* **464**, 1640 (2017).
- [10] J. N. Grieb, A. G. Sánchez, S. Salazar-Albornoz, R. Scoccimarro, M. Crocce, C. Dalla Vecchia, F. Montesano, H. Gil-Marín, A. J. Ross, F. Beutler, S. Rodríguez-Torres, C.-H. Chuang, F. Prada, F.-S. Kitaura, A. J. Cuesta *et al.*, *Mon. Not. R. Astron. Soc.* **467**, 2085 (2017).
- [11] Y. Kobayashi, T. Nishimichi, M. Takada, and H. Miyatake, *Phys. Rev. D* **105**, 083517 (2022).
- [12] C. Hikage, M. Oguri, T. Hamana, S. More, R. Mandelbaum, M. Takada, F. Köhlinger, H. Miyatake, A. J. Nishizawa, H. Aihara, R. Armstrong, J. Bosch, J. Coupon, A. Ducout, P. Ho *et al.*, *Publ. Astron. Soc. Jpn.* **71**, 43 (2019).
- [13] T. Hamana, M. Shirasaki, S. Miyazaki, C. Hikage, M. Oguri, S. More, R. Armstrong, A. Leauthaud, R. Mandelbaum, H. Miyatake, A. J. Nishizawa, M. Simet, M. Takada, H. Aihara, J. Bosch *et al.*, *Publ. Astron. Soc. Jpn.* **72**, 16 (2020).
- [14] C. Heymans, T. Tröster, M. Asgari, C. Blake, H. Hildebrandt, B. Joachimi, K. Kuijken, C.-A. Lin, A. G. Sánchez, J. L. van den Busch, A. H. Wright, A. Amon, M. Bilicki, J. de Jong, M. Crocce *et al.*, *Astron. Astrophys.* **646**, A140 (2021).
- [15] S. Pandey, E. Krause, J. DeRose, N. MacCrann, B. Jain, M. Crocce, J. Blazek, A. Choi, H. Huang, C. To, X. Fang, J. Elvin-Poole, J. Prat, A. Porredon, L. F. Secco *et al.*, *Phys. Rev. D* **106**, 043520 (2022).
- [16] A. Porredon, M. Crocce, J. Elvin-Poole, R. Cawthon, G. Giannini, J. De Vicente, A. Carnero Rosell, I. Ferrero, E. Krause, X. Fang, J. Prat, M. Rodríguez-Monroy, S. Pandey, A. Pocino, F. J. Castander *et al.*, *Phys. Rev. D* **106**, 103530 (2022).
- [17] S. Sugiyama, M. Takada, H. Miyatake, T. Nishimichi, M. Shirasaki, Y. Kobayashi, R. Mandelbaum, S. More, R. Takahashi, K. Osato, M. Oguri, J. Coupon, C. Hikage, B.-C. Hsieh, Y. Komiyama *et al.*, *Phys. Rev. D* **105**, 123537 (2022).
- [18] H. Miyatake, S. Sugiyama, M. Takada, T. Nishimichi, M. Shirasaki, Y. Kobayashi, R. Mandelbaum, S. More,

- M. Oguri, K. Osato, Y. Park, R. Takahashi, J. Coupon, C. Hikage, B.-C. Hsieh *et al.*, *Phys. Rev. D* **106**, 083520 (2022).
- [19] A. Amon, D. Gruen, M. A. Troxel, N. MacCrann, S. Dodelson, A. Choi, C. Doux, L. F. Secco, S. Samuroff, E. Krause, J. Cordero, J. Myles, J. DeRose, R. H. Wechsler, M. Gatti *et al.*, *Phys. Rev. D* **105**, 023514 (2022).
- [20] DES Collaboration, T. M. C. Abbott, M. Aguena, A. Alarcon, S. Allam, O. Alves, A. Amon, F. Andrade-Oliveira, J. Annis, S. Avila, D. Bacon, E. Baxter, K. Bechtol, M. R. Becker, G. M. Bernstein *et al.*, *Phys. Rev. D* **105**, 023520 (2022).
- [21] H. Mo, F. C. van den Bosch, and S. White, *Galaxy Formation and Evolution* (Cambridge University Press, 2010).
- [22] C. L. Bennett, D. Larson, J. L. Weiland, N. Jarosik, G. Hinshaw, N. Odegard, K. M. Smith, R. S. Hill, B. Gold, M. Halpern, E. Komatsu, M. R. Nolte, L. Page, D. N. Spergel, E. Wollack *et al.*, *Astrophys. J. Suppl. Ser.* **208**, 20 (2013).
- [23] J. T. A. de Jong, G. A. Verdoes Kleijn, K. H. Kuijken, and E. A. Valentijn, *Exp. Astron.* **35**, 25 (2013).
- [24] <https://kids.strw.leidenuniv.nl/>.
- [25] The Dark Energy Survey Collaboration, [arXiv:astro-ph/0510346](https://arxiv.org/abs/astro-ph/0510346).
- [26] <https://www.darkenergysurvey.org>.
- [27] H. Aihara, N. Arimoto, R. Armstrong, S. Arnouts, N. A. Bahcall, S. Bickerton, J. Bosch, K. Bundy, P. L. Capak, J. H. H. Chan, M. Chiba, J. Coupon, E. Egami, M. Enoki, F. Finet *et al.*, *Publ. Astron. Soc. Jpn.* **70**, S4 (2018).
- [28] <https://hsc.mtk.nao.ac.jp/ssp/>.
- [29] C. S. Kochanek, [arXiv:astro-ph/0407232](https://arxiv.org/abs/astro-ph/0407232).
- [30] M. Tegmark, M. R. Blanton, M. A. Strauss, F. Hoyle, D. Schlegel, R. Scoccamarro, M. S. Vogeley, D. H. Weinberg, I. Zehavi, A. Berlind, T. Budavari, A. Connolly, D. J. Eisenstein, D. Finkbeiner, J. A. Frieman *et al.*, *Astrophys. J.* **606**, 702 (2004).
- [31] A. Cooray and R. Sheth, *Phys. Rep.* **372**, 1 (2002).
- [32] N. Kaiser, *Astrophys. J. Lett.* **284**, L9 (1984).
- [33] U. Seljak, A. Makarov, R. Mandelbaum, C. M. Hirata, N. Padmanabhan, P. McDonald, M. R. Blanton, M. Tegmark, N. A. Bahcall, and J. Brinkmann, *Phys. Rev. D* **71**, 043511 (2005).
- [34] J. L. Tinker, B. E. Robertson, A. V. Kravtsov, A. Klypin, M. S. Warren, G. Yepes, and S. Gottlöber, *Astrophys. J.* **724**, 878 (2010).
- [35] M. Cacciato, F. C. van den Bosch, S. More, R. Li, H. J. Mo, and X. Yang, *Mon. Not. R. Astron. Soc.* **394**, 929 (2009).
- [36] F. C. van den Bosch, S. More, M. Cacciato, H. Mo, and X. Yang, *Mon. Not. R. Astron. Soc.* **430**, 725 (2013).
- [37] S. More, F. C. van den Bosch, M. Cacciato, A. More, H. Mo, and X. Yang, *Mon. Not. R. Astron. Soc.* **430**, 747 (2013).
- [38] M. Cacciato, F. C. van den Bosch, S. More, H. Mo, and X. Yang, *Mon. Not. R. Astron. Soc.* **430**, 767 (2013).
- [39] S. More, H. Miyatake, R. Mandelbaum, M. Takada, D. N. Spergel, J. R. Brownstein, and D. P. Schneider, *Astrophys. J.* **806**, 2 (2015).
- [40] R. Mandelbaum, A. Slosar, T. Baldauf, U. Seljak, C. M. Hirata, R. Nakajima, R. Reyes, and R. E. Smith, *Mon. Not. R. Astron. Soc.* **432**, 1544 (2013).
- [41] H. Miyatake, S. Sugiyama, M. Takada, T. Nishimichi, X. chong Li, M. Shirasaki, S. More, Y. Kobayashi, A. J. Nishizawa, M. M. Rau, T. Zhang, R. Takahashi, R. Dalal, R. Mandelbaum, M. A. Strauss *et al.*, [arXiv:2304.00704](https://arxiv.org/abs/2304.00704).
- [42] S. Sugiyama, H. Miyatake, S. More, X. Li, M. Shirasaki, M. Takada, Y. Kobayashi, R. Takahashi, T. Nishimichi, A. J. Nishizawa, M. M. Rau, T. Zhang, R. Dalal, R. Mandelbaum, M. A. Strauss *et al.*, [arXiv:2304.00705](https://arxiv.org/abs/2304.00705).
- [43] X. Li, T. Zhang, S. Sugiyama, R. Dalal, M. M. Rau, R. Mandelbaum, M. Takada, S. More, M. A. Strauss, H. Miyatake, M. Shirasaki, T. Hamana, M. Oguri, W. Luo, A. J. Nishizawa *et al.*, [arXiv:2304.00702](https://arxiv.org/abs/2304.00702).
- [44] R. Dalal, X. Li, A. Nicola, J. Zuntz, M. A. Strauss, S. Sugiyama, T. Zhang, M. M. Rau, R. Mandelbaum, M. Takada, S. More, H. Miyatake, A. Kannawadi, M. Shirasaki, T. Taniguchi *et al.*, [arXiv:2304.00701](https://arxiv.org/abs/2304.00701).
- [45] R. Takahashi, T. Hamana, M. Shirasaki, T. Namikawa, T. Nishimichi, K. Osato, and K. Shiroshima, *Astrophys. J.* **850**, 24 (2017).
- [46] S. Miyazaki *et al.*, *Publ. Astron. Soc. Jpn.* **70**, S1 (2018).
- [47] Y. Komiyama, Y. Obuchi, H. Nakaya, Y. Kamata, S. Kawanomoto, Y. Utsumi, S. Miyazaki, F. Uruguchi, H. Furusawa, T. Morokuma, T. Uchida, H. Miyatake, S. Mineo, H. Fujimori, H. Aihara, H. Karoji, J. E. Gunn, and S.-Y. Wang, *Publ. Astron. Soc. Jpn.* **70**, S2 (2018).
- [48] H. Furusawa *et al.*, *Publ. Astron. Soc. Jpn.* **70**, S3 (2018).
- [49] S. Kawanomoto, F. Uruguchi, Y. Komiyama, S. Miyazaki, H. Furusawa, F. Finet, T. Hattori, S.-Y. Wang, N. Yasuda, and N. Suzuki, *Publ. Astron. Soc. Jpn.* **70**, 66 (2018).
- [50] J. Bosch, R. Armstrong, S. Bickerton, H. Furusawa, H. Ikeda, M. Koike, R. Lupton, S. Mineo, P. Price, T. Takata, M. Tanaka, N. Yasuda, Y. AlSayyad, A. C. Becker, W. Coulton *et al.*, *Publ. Astron. Soc. Jpn.* **70**, S5 (2018).
- [51] H. Aihara, R. Armstrong, S. Bickerton, J. Bosch, J. Coupon, H. Furusawa, Y. Hayashi, H. Ikeda, Y. Kamata, H. Karoji, S. Kawanomoto, M. Koike, Y. Komiyama, D. Lang, R. H. Lupton *et al.*, *Publ. Astron. Soc. Jpn.* **70**, S8 (2018).
- [52] H. Aihara, Y. AlSayyad, M. Ando, R. Armstrong, J. Bosch, E. Egami, H. Furusawa, J. Furusawa, A. Goulding, Y. Harikane, C. Hikage, P. T. P. Ho, B.-C. Hsieh, S. Huang, H. Ikeda *et al.*, *Publ. Astron. Soc. Jpn.* **71**, 114 (2019).
- [53] H. Aihara, Y. AlSayyad, M. Ando, R. Armstrong, J. Bosch, E. Egami, H. Furusawa, J. Furusawa, S. Harasawa, Y. Harikane, B.-C. Hsieh, H. Ikeda, K. Ito, I. Iwata, T. Kodama *et al.*, *Publ. Astron. Soc. Jpn.* **74**, 247 (2022).
- [54] X. Li, H. Miyatake, W. Luo, S. More, M. Oguri, T. Hamana, R. Mandelbaum, M. Shirasaki, M. Takada, R. Armstrong, A. Kannawadi, S. Takita, S. Miyazaki, A. J. Nishizawa, A. A. Plazas Malagón *et al.*, *Publ. Astron. Soc. Jpn.* **74**, 421 (2022).
- [55] R. Mandelbaum, H. Miyatake, T. Hamana, M. Oguri, M. Simet, R. Armstrong, J. Bosch, R. Murata, F. Lanusse, A. Leauthaud, J. Coupon, S. More, M. Takada, S. Miyazaki, J. S. Speagle *et al.*, *Publ. Astron. Soc. Jpn.* **70**, S25 (2018).
- [56] R. Mandelbaum, F. Lanusse, A. Leauthaud, R. Armstrong, M. Simet, H. Miyatake, J. E. Meyers, J. Bosch, R. Murata,

- S. Miyazaki, and M. Tanaka, *Mon. Not. R. Astron. Soc.* **481**, 3170 (2018).
- [57] A. J. Nishizawa, B.-C. Hsieh, M. Tanaka, and T. Takata, [arXiv:2003.01511](https://arxiv.org/abs/2003.01511).
- [58] However, the photo- z catalog released for PDR2 is different from the catalog we use in this analysis. We will make the shape catalog, with the photo- z information, publicly available after the cosmology papers are published.
- [59] A self-organizing map is yet another way of characterizing the photometric redshift distribution similar to DEmPz/DNNZ methods. The differences between these methods lie in the machine learning architecture used for the calibration and inference. Please see Rau *et al.* [62] for a detailed discussion about the differences in the calibration strategies adopted in the current surveys.
- [60] M. Oguri and M. Takada, *Phys. Rev. D* **83**, 023008 (2011).
- [61] Although a cut that retains only 24% of source galaxies is quite severe, in these initial rounds of cosmological analyses, we stick to a single source bin at redshifts larger than any of our lens samples to conservatively constrain any systematics in the redshift distribution of the source galaxies and avoid any source galaxies that may be physically correlated with our source galaxies.
- [62] M. M. Rau, R. Dalal, T. Zhang, X. Li, A. J. Nishizawa, S. More, R. Mandelbaum, M. A. Strauss, and M. Takada, [arXiv:2211.16516](https://arxiv.org/abs/2211.16516).
- [63] M. Oguri, *Mon. Not. R. Astron. Soc.* **444**, 147 (2014).
- [64] M. Oguri *et al.*, *Publ. Astron. Soc. Jpn.* **70**, S20 (2018).
- [65] C. Hikage *et al.*, *Publ. Astron. Soc. Jpn.* **71**, 43 (2019).
- [66] <https://www.sdss.org/dr11/>.
- [67] S. Alam, F. D. Albareti, C. Allende Prieto, F. Anders, S. F. Anderson, T. Anderton, B. H. Andrews, E. Armengaud, É. Aubourg, S. Bailey, S. Basu, J. E. Bautista, R. L. Beaton, T. C. Beers, C. F. Bender *et al.*, *Astrophys. J. Suppl. Ser.* **219**, 12 (2015).
- [68] K. S. Dawson *et al.*, *Astron. J.* **145**, 10 (2013).
- [69] H. Miyatake, Y. Kobayashi, M. Takada, T. Nishimichi, M. Shirasaki, S. Sugiyama, R. Takahashi, K. Osato, S. More, and Y. Park, *Phys. Rev. D* **106**, 083519 (2022).
- [70] S. Sugiyama, M. Takada, H. Miyatake, T. Nishimichi, M. Shirasaki, Y. Kobayashi, S. More, R. Takahashi, K. Osato, M. Oguri, J. Coupon, C. Hikage, B.-C. Hsieh, Y. Komiyama, A. Leauthaud *et al.*, [arXiv:2111.10966](https://arxiv.org/abs/2111.10966).
- [71] H. Miyatake, S. More, R. Mandelbaum, M. Takada, D. N. Spergel, J.-P. Kneib, D. P. Schneider, J. Brinkmann, and J. R. Brownstein, *Astrophys. J.* **806**, 1 (2015).
- [72] K. N. Abazajian, J. K. Adelman-McCarthy, M. A. Agüeros, S. S. Allam, C. Allende Prieto, D. An, K. S. J. Anderson, S. F. Anderson, J. Annis, N. A. Bahcall, C. A. L. Bailer-Jones, J. C. Barentine, B. A. Bassett, A. C. Becker, T. C. Beers *et al.*, *Astrophys. J. Suppl. Ser.* **182**, 543 (2009).
- [73] J. E. Gunn, W. A. Siegmund, E. J. Mannery, R. E. Owen, C. L. Hull, R. F. Leger, L. N. Carey, G. R. Knapp, D. G. York, W. N. Boroski, S. M. Kent, R. H. Lupton, C. M. Rockosi, M. L. Evans, P. Waddell *et al.*, *Astron. J.* **131**, 2332 (2006).
- [74] M. Fukugita, T. Ichikawa, J. E. Gunn, M. Doi, K. Shimasaku, and D. P. Schneider, *Astron. J.* **111**, 1748 (1996).
- [75] J. A. Smith, D. L. Tucker, S. Kent, M. W. Richmond, M. Fukugita, T. Ichikawa, S.-i. Ichikawa, A. M. Jorgensen, A. Uomoto, J. E. Gunn, M. Hamabe, M. Watanabe, A. Tolea, A. Henden, J. Annis *et al.*, *Astron. J.* **123**, 2121 (2002).
- [76] M. Doi, M. Tanaka, M. Fukugita, J. E. Gunn, N. Yasuda, Ž. Ivezić, J. Brinkmann, E. de Haars, S. J. Kleinman, J. Krzesinski, and R. French Leger, *Astron. J.* **139**, 1628 (2010).
- [77] D. J. Eisenstein, D. H. Weinberg, E. Agol, H. Aihara, C. Allende Prieto, S. F. Anderson, J. A. Arns, É. Aubourg, S. Bailey, E. Balbinot, R. Barkhouser, T. C. Beers, A. A. Berlind, S. J. Bickerton, D. Bizyaev *et al.*, *Astron. J.* **142**, 72 (2011).
- [78] C. P. Ahn, R. Alexandroff, C. Allende Prieto, S. F. Anderson, T. Anderton, B. H. Andrews, É. Aubourg, S. Bailey, E. Balbinot, R. Barnes, J. Bautista, T. C. Beers, A. Beifiori, A. A. Berlind, V. Bhardwaj *et al.*, *Astrophys. J. Suppl. Ser.* **203**, 21 (2012).
- [79] H. Aihara, C. Allende Prieto, D. An, S. F. Anderson, É. Aubourg, E. Balbinot, T. C. Beers, A. A. Berlind, S. J. Bickerton, D. Bizyaev, M. R. Blanton, J. J. Bochanski, A. S. Bolton, J. Bovy, W. N. Brandt *et al.*, *Astrophys. J. Suppl. Ser.* **193**, 29 (2011).
- [80] R. Lupton, J. E. Gunn, Z. Ivezić, G. R. Knapp, and S. Kent, in *Astronomical Data Analysis Software and Systems X*, Astronomical Society of the Pacific Conference Series Vol. 238, edited by F. R. Jr. Harnden, F. A. Primini, and H. E. Payne (Astronomical Society of the Pacific, 2001), p. 269.
- [81] J. R. Pier, J. A. Munn, R. B. Hindsley, G. S. Hennessy, S. M. Kent, R. H. Lupton, and Ž. Ivezić, *Astron. J.* **125**, 1559 (2003).
- [82] N. Padmanabhan, D. J. Schlegel, D. P. Finkbeiner, J. C. Barentine, M. R. Blanton, H. J. Brewington, J. E. Gunn, M. Harvanek, D. W. Hogg, Ž. Ivezić, D. Johnston, S. M. Kent, S. J. Kleinman, G. R. Knapp, J. Krzesinski *et al.*, *Astrophys. J.* **674**, 1217 (2008).
- [83] D. J. Schlegel, D. P. Finkbeiner, and M. Davis, *Astrophys. J.* **500**, 525 (1998).
- [84] A. S. Bolton, D. J. Schlegel, É. Aubourg, S. Bailey, V. Bhardwaj, J. R. Brownstein, S. Burles, Y.-M. Chen, K. Dawson, D. J. Eisenstein, J. E. Gunn, G. R. Knapp, C. P. Loomis, R. H. Lupton, C. Maraston *et al.*, *Astron. J.* **144**, 144 (2012).
- [85] B. Reid, S. Ho, N. Padmanabhan, W. J. Percival, J. Tinker, R. Tojeiro, M. White, D. J. Eisenstein, C. Maraston, A. J. Ross, A. G. Sánchez, D. Schlegel, E. Sheldon, M. A. Strauss, D. Thomas *et al.*, *Mon. Not. R. Astron. Soc.* **455**, 1553 (2016).
- [86] L. Anderson, É. Aubourg, S. Bailey, F. Beutler, V. Bhardwaj, M. Blanton, A. S. Bolton, J. Brinkmann, J. R. Brownstein, A. Burden, C.-H. Chuang, A. J. Cuesta, K. S. Dawson, D. J. Eisenstein, S. Escoffier *et al.*, *Mon. Not. R. Astron. Soc.* **441**, 24 (2014).
- [87] H. Guo, I. Zehavi, and Z. Zheng, *Astrophys. J.* **756**, 127 (2012).
- [88] D. A. Wake, R. C. Nichol, D. J. Eisenstein, J. Loveday, A. C. Edge, R. Cannon, I. Smail, D. P. Schneider, R. Scranton, D. Carson, N. P. Ross, R. J. Brunner, M. Colless, W. J. Couch, S. M. Croom *et al.*, *Mon. Not. R. Astron. Soc.* **372**, 537 (2006).

- [89] G. Bruzual and S. Charlot, *Mon. Not. R. Astron. Soc.* **344**, 1000 (2003).
- [90] A. J. Ross, W. J. Percival, A. G. Sánchez, L. Samushia, S. Ho, E. Kazin, M. Manera, B. Reid, M. White, R. Tojeiro, C. K. McBride, X. Xu, D. A. Wake, M. A. Strauss, F. Montesano *et al.*, *Mon. Not. R. Astron. Soc.* **424**, 564 (2012).
- [91] The gap in the redshift distributions between LOWZ and CMASS samples is due to our use of the SDSS DR11 parent sample. Using the latest DR12 catalog would have allowed us to add in a few more galaxies at intermediate redshifts. However, that would have required us to modify the BOSS large-scale structure sample to include the fiber collided and redshift failure galaxies. Since this procedure was already performed for DR11, we decided to stick with this sample.
- [92] G. Hinshaw, D. Larson, E. Komatsu, D. N. Spergel, C. L. Bennett, J. Dunkley, M. R. Nolta, M. Halpern, R. S. Hill, N. Odegard, L. Page, K. M. Smith, J. L. Weiland, B. Gold, N. Jarosik *et al.*, *Astrophys. J. Suppl. Ser.* **208**, 19 (2013).
- [93] M. Shirasaki, T. Hamana, M. Takada, R. Takahashi, and H. Miyatake, *Mon. Not. R. Astron. Soc.* **486**, 52 (2019).
- [94] J. F. Navarro, C. S. Frenk, and S. D. M. White, *Astrophys. J.* **490**, 493 (1997).
- [95] P. S. Behroozi, R. H. Wechsler, and H.-Y. Wu, *Astrophys. J.* **762**, 109 (2013).
- [96] The original code was written in C++ by Matthew B Kennel; the first author of this paper has carried out some bug fixes, memory leaks and optimizations.
- [97] C. Hikage, M. Takada, T. Hamana, and D. Spergel, *Mon. Not. R. Astron. Soc.* **412**, 65 (2011).
- [98] M. A. Troxel *et al.* (DES Collaboration), *Phys. Rev. D* **98**, 043528 (2018).
- [99] T. Zhang, X. Li, R. Dalal, R. Mandelbaum, M. A. Strauss, A. Kannawadi, H. Miyatake, A. Nicola, A. A. Plazas Malagón, M. Shirasaki, S. Sugiyama, and M. Takada, [arXiv:2212.03257](https://arxiv.org/abs/2212.03257).
- [100] J. Hartlap, P. Simon, and P. Schneider, *Astron. Astrophys.* **464**, 399 (2007).
- [101] Note that unlike cosmic shear covariance, there is no mixed term between large structure and shape noise in the galaxy-galaxy lensing measurements.
- [102] T. Hamana, M. Shirasaki, S. Miyazaki, C. Hikage, M. Oguri, S. More, R. Armstrong, A. Leauthaud, R. Mandelbaum, H. Miyatake, A. J. Nishizawa, M. Simet, M. Takada, H. Aihara, J. Bosch, Y. Komiyama, R. Lupton, H. Murayama, M. A. Strauss, and M. Tanaka, *Publ. Astron. Soc. Jpn.* **72**, 16 (2020).
- [103] One may think that the factor of 1.08 is not enough because the blue contour does not cover the green contour in Fig. 18. Depending on the flags, `i_calib_psf_used=True` or `False`, we not only use different coefficients but also different $\xi_{pp,qq}^{pp,qq}$, and the difference is not so significant in predicted $\hat{\xi}_{pp,qq}^{psf}$ than how it appears in Fig. 18.
- [104] <http://dm.lsst.org>.